

Electronic Theses and Dissertations, 2004-2019

2014

Computational Fluid Dynamics Simulation of United Launch Alliance Delta IV Hydrogen Plume Mitigation Strategies

Stephen Guimond
University of Central Florida

 Part of the [Mechanical Engineering Commons](#)
Find similar works at: <https://stars.library.ucf.edu/etd>
University of Central Florida Libraries <http://library.ucf.edu>

This Masters Thesis (Open Access) is brought to you for free and open access by STARS. It has been accepted for inclusion in Electronic Theses and Dissertations, 2004-2019 by an authorized administrator of STARS. For more information, please contact STARS@ucf.edu.

STARS Citation

Guimond, Stephen, "Computational Fluid Dynamics Simulation of United Launch Alliance Delta IV Hydrogen Plume Mitigation Strategies" (2014). *Electronic Theses and Dissertations, 2004-2019*. 4590. <https://stars.library.ucf.edu/etd/4590>

COMPUTATIONAL FLUID DYNAMICS SIMULATION OF UNITED
LAUNCH ALLIANCE DELTA IV HYDROGEN PLUME MITIGATION
STRATEGIES

by

STEPHEN A. GUIMOND
B.S. of Mechanical Engineering
University of Central Florida, 2012

A thesis submitted in partial fulfillment of the requirements
for the degree of Master of Science in Mechanical Engineering
in the Department of Mechanical and Aerospace Engineering
in the College of Engineering and Computer Science
at the University of Central Florida
Orlando, Florida

Fall Term

2014

Major Professor: Alain Kassab

The material presented in this paper was approved for public release by the Department of Defense Office of Prepublication and Security Review on October 28, 2014. The approval does not include any photograph, picture, exhibit, caption or other supplemental material not specifically approved by the DoD. This release does not imply DoD endorsement or factual accuracy of the material.

ABSTRACT

During the launch sequence of the United Launch Alliance Delta IV launch vehicle, large amounts of pure hydrogen are introduced into the launch table and ignited by Radial-Outward-Firing-Igniters (ROFIs). This ignition results in a significant flame, or plume, that rises upwards out of the launch table due to buoyancy. The presence of the plume causes increased and unwanted heat loads on the surface of the vehicle. A proposed solution is to add a series of fans and structures to the existing launch table configuration that are designed to inject ambient air in the immediate vicinity of the launch vehicle's nozzles to suppress the plume rise. In addition to the air injection, secondary fan systems can be added around the launch table openings to further suppress the hydrogen plume. The proposed air injection solution is validated by computational fluid dynamics simulations that capture the combustion and compressible flow observed during the Delta IV launch sequence. A solution to the hydrogen plume problem will have direct influence on the efficiency of the launch vehicle: lower heat loads result in thinner vehicle insulation and thus allow for a larger payload mass. Current results show that air injection around the launch vehicle nozzles and air suppression around the launch table openings significantly reduces the size of the plume around the launch vehicle prior to liftoff.

ACKNOWLEDGMENTS

I would like to thank my parents for supporting me throughout my academic career and as a result of this support I was able to focus on my studies. I would also like to thank Dr. Alain Kassab for taking me on as an undergraduate research student and exposing me to a variety of research projects. Additionally, I want to thank Sebastian Sotelo, Marcus Ni, and Nicholas Voce for their help with the Delta IV hydrogen plume project. Finally, I would like to thank United Launch Alliance, Si Song, and Zachary Richards for the opportunity to work on such an interesting problem.

TABLE OF CONTENTS

LIST OF FIGURES	vii
LIST OF TABLES	x
CHAPTER 1: INTRODUCTION	1
Outline of Study	2
CHAPTER 2: METHODS	6
Flow Physics	6
Discrete Transfer Radiation Model (DTRM)	11
P-1 Radiation Model	12
Rosseland Radiation Model	13
Discrete Ordinates (DO) Radiation Model	13
Mesh Generation	14
CHAPTER 3: RESULTS	20
Reduced VAFB Model	20
Air Injection Inclination Comparison	21
Air Injection Flow Rate Comparison	23
Air Curtain Flow Rate Determination	26
Reduced VAFB Model Conclusions	29
Full Scale VAFB Model	31

1.6x Base Flow Rate Air Injection.....	32
Base Flow Rate Air Injection and Air Curtain.....	37
Base Flow Rate Air Injection and Venturi.....	41
Base Flow Rate Air Injection, Air Curtain and Venturi	45
Case Comparison with No Mitigation Present.....	49
CHAPTER 4: DISCUSSION AND CONCLUSIONS	57
Reduced Model Results.....	57
Full Scale Model Results.....	59
REFERENCES	63

LIST OF FIGURES

Figure 1: Flame produced during the Delta IV Heavy launch sequence.	3
Figure 2: Vandenberg Air Force Base (VAFB) launch pad geometry.	15
Figure 3: Reduced VAFB launch pad geometry.	16
Figure 4: Single engine VAFB tetrahedral mesh.	17
Figure 5: Full scale VAFB tetrahedral mesh.	17
Figure 6: Air curtain geometry (shown in red).	18
Figure 7: VAFB flame trench section with venturi system.	19
Figure 8: VAFB flame trench section without venturi system.	19
Figure 9: Hydrogen plume rise for the base inclination angle (left) and 2.5x base inclination angle (right) air injection simulations.	22
Figure 10: Hydrogen plume rise for 0.5x base flow rate (left) and base flow rate (right) air injection simulations.	25
Figure 11: Hydrogen plume rise for 0.5x base flow rate (left), base flow rate (center), and 1.6x base flow rate (right) air curtain simulations.	27
Figure 12: Launch table aspiration.	29
Figure 13: Hydrogen plume rise for base air flow rate injection with 1.6x base flow rate air curtain (left) and no injection (right).	30
Figure 14: Hydrogen plume rise for the 1.6x base air injection case.	34
Figure 15: Surface temperature contour plots for the 1.6x base air flow rate injection case.	35
Figure 16: Additional surface temperature contour plots for the 1.6x base air injection case.	36

Figure 17: Hydrogen plume rise for the base air injection flow rate and base air curtain flow rates.....	38
Figure 18: Surface temperature contour plots for the base air injection and base air curtain flow rates.....	39
Figure 19: Additional surface temperature contour plots for the base air injection and base air curtain flow rates.....	40
Figure 20: Hydrogen plume rise for the base air injection and venturi case.	42
Figure 21: Surface temperature contour plots for the base air injection and venturi case.....	43
Figure 22: Additional surface temperature contour plots for the base air injection and venturi case.....	44
Figure 23: Hydrogen plume rise for the base flow rate air injection, curtain and venturi case....	46
Figure 24: Surface temperature contour plots for the base flow rate air injection, curtain and venturi case.	47
Figure 25: Additional surface temperature contour plots for the base flow rate air injection, curtain and venturi case	48
Figure 26: Hydrogen plume rise for the no injection case.....	50
Figure 27: Surface temperature contour plots for the no injection case.	51
Figure 28: Additional surface temperature contour plots for the no injection case.....	52
Figure 29: Surface temperature contour plot comparison for the base air injection and venturi case (left column) and the no injection case (right column).....	54
Figure 30: Surface temperature contour plot comparison between the base air injection, air curtain and venturi case (left column) and the no injection case (right column).....	55

Figure 31: Hydrogen plume rise comparison for the base air injection and venturi case (top left), base air injection, air curtain and venturi case (bottom left) and the no injection case (right). 56

Figure 32: The hydrogen plume (left) and launch vehicle surface temperatures (center, right) for Case 3 in Table 2..... 60

Figure 33: The hydrogen plume (left) and launch vehicle surface temperatures (center, right) for Case 4 in Table 2..... 61

LIST OF TABLES

Table 1: Summary of reduced model cases completed.....	21
Table 2: Summary of the full scale cases analyzed.	32

CHAPTER 1: INTRODUCTION

Liquid hydrogen/liquid oxygen (LH₂/LOX) based rocket engines have had widespread use in the past and perhaps made famous by NASA's Space Shuttle Main Engine. LH₂ is a very effective propellant and is able to deliver a very high specific impulse when compared to other hydrocarbon fuels [8]. In addition, the combustion products of LH₂/LOX combustion are clean and free of any harsh chemicals. Other fuel and oxidizer combinations, such as Fluorine and Hydrazine, are able to deliver specific impulses near that of LH₂/LOX engines but produce toxic byproducts. Hydrogen is not without its drawbacks, however. The low density of liquid hydrogen means that for the same launch vehicle volume, less hydrogen can be carried than a hydrocarbon based fuel. The buoyancy of the reactants and combustion products for LH₂/LOX engines create a rising flame, as seen in the United Launch Alliance (ULA) Delta IV launch vehicle (Figure 1). The same flame is not present during the launch of the ULA Atlas V launch vehicle, which is powered by kerosene and liquid oxygen. The hydrogen plume created by the Delta IV and its mitigation is the target of this study.

Along with the details just mentioned, Hydrogen carries the potential for detonation and this potential needs to be addressed if a Hydrogen powered vehicle is to launch safely. In the case of the Space Shuttle, the possibility of excess unburned Hydrogen detonation during launch (and abort scenarios) was eliminated by adding large amounts of superheated water into the launch structure to create a mixture unable to hold a flame. A computational fluid dynamics (CFD) simulation was carried out on the Vandenberg Space Shuttle launch site [9] assessing the effectiveness of the Steam Inerting System (SIS) that made use of the Equation Independent

Transient Analysis Computer Code (EITACC). EITACC is a pressure dependent code that includes the relevant physical phenomena: combustion, subsonic and supersonic flow, multiphase flow, and the vaporization of the superheated steam. It should be noted that the Cape Canaveral launch site was less of a concern due to the fact that the launch duct geometry is open while the Vandenberg site has closed duct geometry. The SIS has the additional role of damping acoustic vibrations, or ignition overpressure waves (IOP), emanating from the Space Shuttle Main Engines (SSMEs) and solid rocket boosters (SRBs) that have the potential to harm the launch vehicle. Numerical studies into the water suppression technique are given in [11, 13] and an analytical model for the IOP phenomena is presented in [12]. The results of the SIS CFD simulations showed that the superheated steam was effective at rendering the Hydrogen/Air/Water Vapor mixture inert. The EITACC results were compared with a 1/7th scale test of the Vandenberg launch site exhaust duct [10] and were shown to support this conclusion. Interestingly, the results from the 1/7th scale test show that all of the conditions evaluated result in a safe duct environment.

Outline of Study

United Launch Alliance offers several different sized launch vehicles and launch vehicle configurations for the Delta IV to launch a given payload into orbit. The available vehicles range from a single booster core setup (Delta IV Medium) that have the potential for additional thrust via small solid rocket boosters (Delta IV Medium+) to a large, three booster launch vehicle (Delta IV Heavy) capable of lifting heavy payloads. Each variant is powered by a liquid hydrogen/liquid oxygen engine for the first stage. During the launch sequence, large amounts of unburned hydrogen are exhausted from the engines and introduced into the launch table. Prior to

engine start, igniters initiate a reaction between the unburned hydrogen and the atmospheric air, producing a flame. The density differential between the flame and its surroundings cause the reaction products to rise upwards out of the launch table, producing the situation shown in Figure 1. The presence of this flame near the launch vehicle causes unwanted heat loads and even has the possibility of charring the external insulation. It is of interest to investigate potential launch table additions to address this problem.



Figure 1: Flame produced during the Delta IV Heavy launch sequence.

The intent of this study was to explore several different strategies aimed at mitigating the flame produced by the Delta IV Heavy engine start sequence. The Delta IV Medium and Medium+ variants also produce a hydrogen plume but are not as pronounced as the Heavy. The investigation was carried out by running computational fluid dynamics (CFD) simulations in ANSYS FLUENT. Each simulation captured the transient hydrogen/oxygen combustion and buoyancy driven plume rise observed in the real world situation. A radiation model was included

due to the large temperatures produced during combustion. The simulations were run in parallel at the Computational Mechanics Laboratory (CML) at the University of Central Florida on Intel Xeon CPUs running at 2.90 GHz. Each simulation was run on approximately 48 CPUs.

Several different strategies were proposed for dealing with the hydrogen plume problem. All of the strategies centered on introducing atmospheric air to oppose the rising flame and create a suction effect inside of the launch table. An air injection system was to be installed around the launch vehicle's convergent-divergent nozzles to push the buoyant flame downwards. Potential air injection geometry was produced in Solidworks and added to the launch table geometry. The second mitigation strategy studied was an air curtain system to be installed on the periphery of the launch table. As the flame rises out of various exits present on the launch table, the air curtain system blows the rising plume away from the launch vehicle. Like the air injection system, the air curtain system delivers atmospheric air at high velocities. The final plume mitigation strategy studied was a venturi system to be installed inside of the flame trenches. The venturi system pushes a large amount of air at a lower velocity out of the exit of the flame trenches. A suction effect is created by this bulk air motion intended to supplement the suction created by the air injection system further upstream.

Vastly differing length scales on the launch vehicle lead to a very sizeable computational mesh so in the interest of time, the full scale model was initially reduced to a single engine model and a partial flame trench. The reduced model resulted in a much smaller overall mesh that had the ability to produce results fairly quickly. This reduced model was used to test the effectiveness of different air flow rates and geometry configurations and the results were to be

applied to the full scale model. The results of the study are presented beginning with the computational model selection and computational mesh generation of both the reduced and full scale models. The findings for the reduced model and the full scale model are then presented respectively in increasing complexity.

CHAPTER 2: METHODS

Flow Physics

ANSYS FLUENT is a finite volume code and solves the conservation equations in the integral formulation. For a general scalar ϕ , the transport equation is given by (1). The volume integrals in the transport equation are discretized for each element and the surface integrals are discretized for each control volume face. The result of the discretization is shown in (2).

$$\int \frac{\partial(\rho\phi)}{\partial t} dV + \oint \rho\phi\vec{v} \cdot d\vec{A} = \oint \Gamma_{\phi} \nabla\phi \cdot d\vec{A} + \int S_{\phi} dV \quad (1)$$

$$\frac{\partial(\rho\phi)}{\partial t} V + \sum_f^{N_{faces}} \rho_f \phi_f \vec{v}_f \cdot \vec{A}_f = \sum_f^{N_{faces}} \Gamma_{\phi} \nabla\phi_f \cdot \vec{A}_f + S_{\phi} V \quad (2)$$

Note that ρ is the fluid density, t is time, V is a general control volume, A is a general surface area, Γ_{ϕ} is the diffusion coefficient for ϕ , and S_{ϕ} is the source term for ϕ . A subscript f denotes evaluation on a per face basis. Two numerical schemes are available to solve the discretization provided by (2): the pressure based and density based solvers. In the past, the density based solver was restricted to high speed compressible flows while the pressure based solver was restricted to low speed incompressible flows. Currently, however, both schemes have been adapted to work with either flow regime. The density based scheme solves all of the conservation equations in an iterative and coupled manner. At each iteration after the properties have been calculated, other scalar equations (like the radiative transfer equation) are solved and the solution is checked for convergence. Both implicit and explicit coupling is available in the density based solver. The pressure based solver is a segregated solver but a coupled version is available. In the segregated implementation, the properties are solved one after another; a pressure correction

equation is solved and properties are updated. Then, the other scalar equations are solved and the solution is checked for convergence. Due to the segregated nature of the pressure based solver, it is more memory efficient than the density based solver but slower to converge. In the coupled implementation of the pressure based solver, the conservation equations are coupled and thus a pressure correction equation is not required. This allows for a faster convergence speed at the cost of a memory increase: an approximate 1.5 – 2 fold increase [3]. Since the pressure based solver was intended for subsonic flows and most of the computational domain is subsonic, the pressure based solver was chosen for this study. Specifically, the pressure based, PISO velocity coupling solver was used. In the last few seconds of the launch sequence, flow through the launch vehicle nozzles become supersonic and the pressure based solver is able to handle the transition.

Due to the large velocities delivered by both the plume mitigation geometry and the launch vehicle nozzles, the flow is inherently turbulent. ANSYS FLUENT offers many different turbulence models including the Spalart-Allmaras Model, the k- ϵ model (Standard, RNG and Realizable), the k- ω model (Standard and SST) and others each having their own strengths and weaknesses. The most widely used turbulence models are the k- ϵ and k- ω models which are both semi-empirical. The k- ω model excels in the near wall region and requires that the mesh be fine enough to accurately resolve the boundary layer. The k- ϵ model uses empirical wall functions based on flat plate flows to calculate near wall behavior and thus isn't as accurate when compared to the k- ω model. The k- ϵ model does not have the boundary resolution requirement that the k- ω model has and thus coarser meshes can be used.

The Shear Stress Transport $k-\omega$ model is an improvement over the standard $k-\omega$ in that it blends the $k-\omega$ with the $k-\epsilon$ model. Near wall behavior is accurately handled by the $k-\omega$ model and core turbulent flow is handled by the $k-\epsilon$ model. The models are connected by a blending function that takes on a value of 1 at the near wall region and 0 in the core flow. Each model introduces scalar transport equations for ϵ , ω , and k which are solved after the main flow parameters (velocity, pressure, etc.) as noted in the numerical solver discussion above. The regions of interest in this study were far removed from any walls and thus the Realizable $k-\epsilon$ turbulence model was chosen.

During the transient launch vehicle start sequence, a wide range of temperatures are present. Temperature changes were too large to be ignored and thus thermal and fluid properties must be assumed as functions of temperature. The specific heat, thermal conductivity and viscosity of each constituent species were allowed to vary as a function of temperature, specifically as a fourth order polynomial. Polynomial coefficients were taken from FLUENT's internal database which was compiled based on values taken from both [4] and [5]. The properties of the mixture of gases were calculated with a mass weighted mixing law based on the individual species. The compressible flow seen in the later stages of the launch vehicle start sequence require that the overall mixture of gases be treated as an ideal gas.

The combustion occurring in the launch vehicle combustion chamber was not calculated by FLUENT. The amount of hydrogen and oxygen introduced into the combustion chamber was provided by the engine manufacturer and assumed to combust in a single step. The calculated amounts of hydrogen, oxygen and water vapor were then applied to the inlets of the converging-diverging nozzles on the launch vehicle along with stagnation temperature, also provided by the

engine manufacturer. Flow was then allowed to expand and combust according to the combustion model detailed below.

When FLUENT's species transport and combustion models are enabled, another series of equations must be included to conserve individual species. In general, for species i , the conservation equation is

$$\frac{\partial(\rho Y_i)}{\partial t} + \nabla \cdot (\rho \bar{v} Y_i) = -\nabla \cdot \vec{J}_i + R_i + S_i \quad (3)$$

In (3), ρ is density, Y is species mass fraction, v is velocity, J is the species diffusive flux, R is the species creation/destruction rate, and S can be a user defined source. For turbulent flows, the species diffusive flux includes the classical Fickian component as well as a turbulent component and is given by

$$\vec{J}_i = -(\rho D_{i,m} + \frac{\mu_t}{Sc_t}) \nabla Y_i \quad (4)$$

In (4), $D_{i,m}$ is the diffusion coefficient for species i in the mixture, μ_t is the turbulent viscosity and Sc_t is the turbulent Schmidt number ($\frac{\mu_t}{\rho D_t}$ where D_t is the turbulent diffusivity). For turbulent flows, the turbulent diffusion contribution to J is generally larger than the laminar (Fickian) contribution.

FLUENT offers several combustion models that include a Laminar Finite Rate model, Eddy Dissipation model, Eddy Dissipation Concept model, and a combination Finite Rate/Eddy Dissipation model. The Laminar Finite Rate model, as the name suggests, is exact for laminar flames and ignores any turbulence present in the flow and chemical rates for each of the species are determined by Arrhenius expressions. In the Eddy Dissipation model, the chemical rates are

controlled only by turbulence and the Arrhenius rates are not considered. The Eddy Dissipation Concept allows detailed chemical kinetic mechanisms to be incorporated into turbulent flows. FLUENT also has the ability to import a CHEMKIN reaction mechanism however detailed chemical kinetics information, such as radical concentration, was not desired and so the combustion calculation was carried out by using ANSYS FLUENT's Finite Rate/Eddy-Dissipation combustion model. This model calculates both the finite reaction rate and the reaction rate due to turbulent mixing and uses the smaller of the two for the overall reaction rate. Fuels are generally fast burning and are limited by turbulent mixing. In general, the finite reaction rate for reaction r and species i is given by (5).

$$R_{i,r} = \Gamma(v_i'' - v_i') \left\{ k_f \prod_{j=1}^N [C_j]^{\eta_j' + \eta_j''} \right\} \quad (5)$$

Note that Γ is the third body effect coefficient, v' and v'' are the stoichiometric coefficient for reactant and product i in reaction r respectively, k_f is the forward rate constant, C_j is the molar concentration of species j, and η' and η'' are the rate exponents for reactants and products in reaction r, respectively. In (5), the forward rate constant for a specific reaction is given by

$$k_f = AT^B e^{-E/RT} \quad (6)$$

A and B are the pre-exponential and temperature coefficient respectively, E is the activation energy, T is the temperature and R is the universal gas constant. All values vary based on the specific reaction considered. ANSYS FLUENT calculates the turbulent reaction rate based on the work of Magnussen [1,14], given by (7) and (8). The smaller of the two reaction rates is used for comparison against the finite rate, given above.

$$R_{i,r} = v_{i,r}' MW_i A \rho \frac{\varepsilon}{k} \min\left(\frac{Y_R}{v_{R,r}' MW_R}\right) \quad (7)$$

$$R_{i,r} = v_{i,r}' MW_i A B \rho \frac{\varepsilon}{k} \frac{\sum_P Y_P}{\sum_j^N v_{j,r}'' MW_j} \quad (8)$$

MW_i signifies the molecular weight of species i , A and B are empirical constants equal to 4.0 and 0.5 respectively, ε and k are the turbulent dissipation rate and turbulent kinetic energy, ρ is the fluid density, and Y_R and Y_P are the mass fractions of a specific reactant or product species. The reactions are assumed to occur in a single step and the parameters in (5) and (6) are chosen to be an engineering approximation of the overall reaction mechanism. Such single step parameters for various reactions have been determined and a table of reaction rate parameters for various hydrocarbons is included in [7].

Due to the large flame temperatures typical of hydrogen combustion, thermal radiation is an important mode of heat transfer. ANSYS FLUENT offers several radiation models: Discrete Transfer Radiation Model (DTRM), P-1 Radiation Model, Rosseland Model, Surface to Surface (S2S) Radiation Model and the Discrete Ordinates (DO) Radiation Model.

Discrete Transfer Radiation Model (DTRM)

The basic assumption of the DTRM is that the radiation leaving surface elements in a certain range of solid angles can be approximated by a single ray. Along that ray (ds), the change of radiation intensity (dI) is given by

$$\frac{dI}{ds} + aI = \frac{a\sigma T^4}{\pi} \quad (9)$$

Note that “a” is the gas absorption coefficient, σ is the Stefan-Boltzmann constant and T is the gas temperature. Equation (9) is integrated along rays starting at boundary faces. DTRM is a relatively simple model and the accuracy can be controlled by the user by increasing the number of rays traced. Radiation is assumed gray, surfaces are assumed diffuse and DTRM is compatible with a large range of optical thicknesses (aL where L is a reference length). As seen in (9), the scattering effect is not taken into consideration. Unfortunately, FLUENT’s implementation of DTRM is not compatible with parallel processing. Due to the large mesh sizes used in this study, parallel processing is required.

P-1 Radiation Model

The P-1 model is derived from the more general P-N model which expands the radiation intensity into a series of spherical harmonics and the P-1 model only uses the first four terms. In this model, the radiation heat flux q_r is given in terms of the incident radiation as

$$q_r = -\frac{1}{3(a + \sigma_s) - C\sigma_s} \nabla G \quad (10)$$

C is involved in radiation scattering and is the linear-anisotropic phase function coefficient and σ_s is the radiation scattering coefficient. A parameter Γ can be defined as

$$\Gamma = \frac{1}{3(a + \sigma_s) - C\sigma_s} \quad (11)$$

The transport equation for the incident radiation is given as

$$\nabla \cdot (\Gamma \nabla G) - aG + 4a\sigma T^4 = S_G \quad (12)$$

In (12), S_G can be a user defined radiation source. Just like DTRM, the P-1 model assumes gray radiation. The P-1 model also assumes all surfaces in the computational domain are diffuse. Since the radiative transfer equation is a diffusion equation, it is easier to solve and thus less CPU intensive.

Rosseland Radiation Model

The Rosseland model handles radiation heat flux similar to the P-1 model except that it assumes the intensity is the black body intensity at the local gas temperature. Specifically,

$$q_r = -16\sigma\Gamma n^2 T^3 \nabla T \quad (13)$$

In (13), n is the refractive index of the gas. This means that a transport equation for G does not need to be solved and thus the Rosseland model has a smaller CPU and memory footprint than that of the P-1 model. The same parameter Γ is used in the Rosseland model so it can handle anisotropic scattering. The Rosseland model's approximation is only valid for optically thick media where absorption plays a large role in the heat transfer process. The derivation of the Rosseland heat flux (or Rosseland diffusion equation), (13), is covered in [6].

Discrete Ordinates (DO) Radiation Model

The DO model can handle a large range of optical thicknesses and can also handle both gray and non-gray radiation for participating media. A radiative transfer equation, (14), is written to solve for the radiation intensity, I , in the participating media. The discrete ordinates model rewrites the radiative transfer equation into a field equation, (15), and is solved for a finite number of solid angles determined by the user.

$$\frac{dI(\vec{r}, \vec{s})}{ds} + (a + \sigma_s)I(\vec{r}, \vec{s}) = an^2 \frac{\sigma T^4}{\pi} + \frac{\sigma_s}{4\pi} \int_0^{4\pi} I(\vec{r}, \vec{s}') \Phi(\vec{s} \cdot \vec{s}') d\Omega' \quad (14)$$

$$\nabla \cdot I(\vec{r}, \vec{s}) + (a + \sigma_s)I(\vec{r}, \vec{s}) = an^2 \frac{\sigma T^4}{\pi} + \frac{\sigma_s}{4\pi} \int_0^{4\pi} I(\vec{r}, \vec{s}') \Phi(\vec{s} \cdot \vec{s}') d\Omega' \quad (15)$$

Note that I is the radiation intensity, \vec{r} is the position vector, \vec{s} is the direction vector, \vec{s}' is the scattering direction vector, s is the path length, a is the absorption coefficient, n is the refractive index, σ_s is the scattering coefficient, σ is the Stefan-Boltzmann constant, T is the temperature, Φ is the scattering phase function and Ω' is the solid angle. The non-gray implementation in the DO model allows the user to specify discrete wavelength bands. The behavior within each band is assumed gray; properties are constant across the discrete wavelength band. The DO model was deemed the most appropriate for this combustion application; it is a robust model that can handle the entire range of optical thicknesses, it is compatible with parallel processing, and [3] cites that it has modest computational costs. Each octant of angular space had 2 divisions in both the θ and ϕ directions which resulted in a total of 32 directions to be solved. Absorption coefficient values were taken from [2] and averaged over the expected temperature. The absorption coefficient was assumed to have no spectral dependence and all radiation was assumed diffuse.

Mesh Generation

The geometry for the Vandenberg Air Force Base launch site (Figure 2) was provided by United Launch Alliance and imported into Gridgen Pointwise v16 for manipulation. The final mesh was projected to contain a large amount of elements. The large mesh size coupled with large transient timeframe results in long simulation run times, even with parallel processing. In order to determine what types of flow rates and plume mitigation geometries would prove most effective,

it was decided that the Delta IV Heavy launch vehicle, consisting of 3 engines, would be stripped down to a single engine. It was assumed that an effective plume mitigation strategy for a single engine would be effective for the full, 3 engine Heavy configuration. The smaller geometry size would allow for much quicker simulation run times. Once air flow rates and mitigation geometry were chosen they would be applied to the full size model.

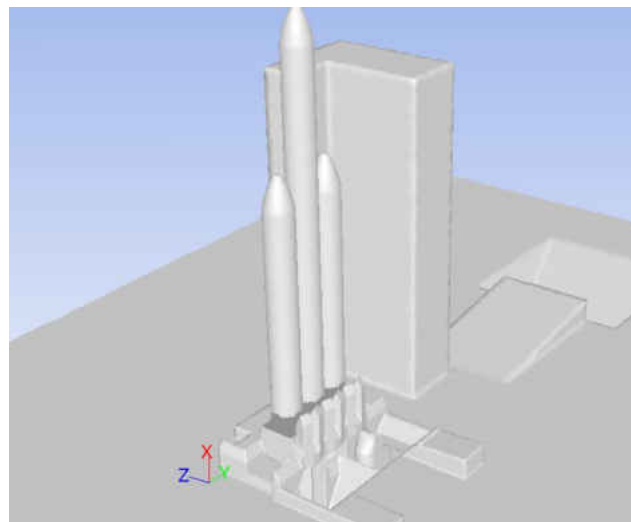


Figure 2: Vandenberg Air Force Base (VAFB) launch pad geometry.

Unfortunately, the launch vehicle engine exhaust is not symmetrically split between the three engines. The central and one exterior booster (in the foreground of Figure 2) are channeled to exhaust in one direction and the remaining booster exhausts in the other direction. This means that reducing the geometry to a single engine could eliminate the coupled plume generation effect one engine has on another. In order to reduce this error, it was chosen that the full scale Delta IV Heavy geometry would be reduced down to the single booster that vented into its own flame trench, specifically the booster in the background of Figure 2. The reduced model is shown below in Figure 3.

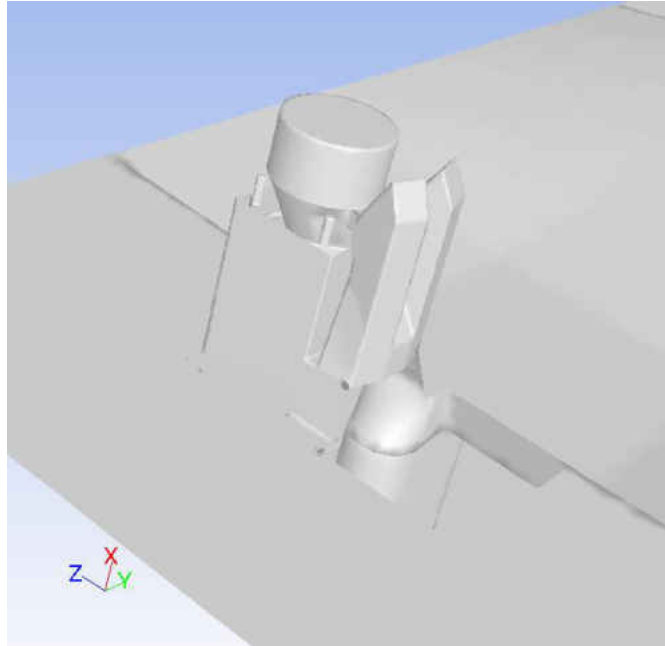


Figure 3: Reduced VAFB launch pad geometry.

Due to the unconventional geometry, an unstructured tetrahedral mesh was chosen to fill the volume. Particular care was taken to minimize the number of high aspect ratio elements and to reduce the skewness of the overall mesh. The vast majority of the computational grid is concentrated in the enclosed engine section where the excess hydrogen is introduced into the launch table. The minimum element edge length was dictated by the smallest port on the underside of the launch vehicle and the mesh was grown at an appropriate rate outward. In order to reduce the overall mesh size, very large element edge lengths were used for the ambient region far from the launch vehicle. The mesh was split into a number of connected blocks to facilitate ease of troubleshooting and mesh quality assessment. The single engine mesh is shown in Figure 4 while the full scale VAFB mesh is shown in Figure 5. The single engine mesh sizes were on the order of 4 million cells while the full scale models averaged around 14 million cells.

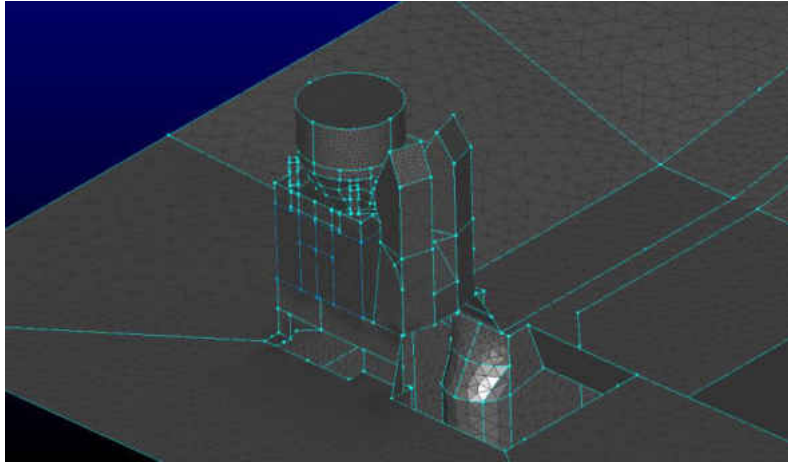


Figure 4: Single engine VAFB tetrahedral mesh.

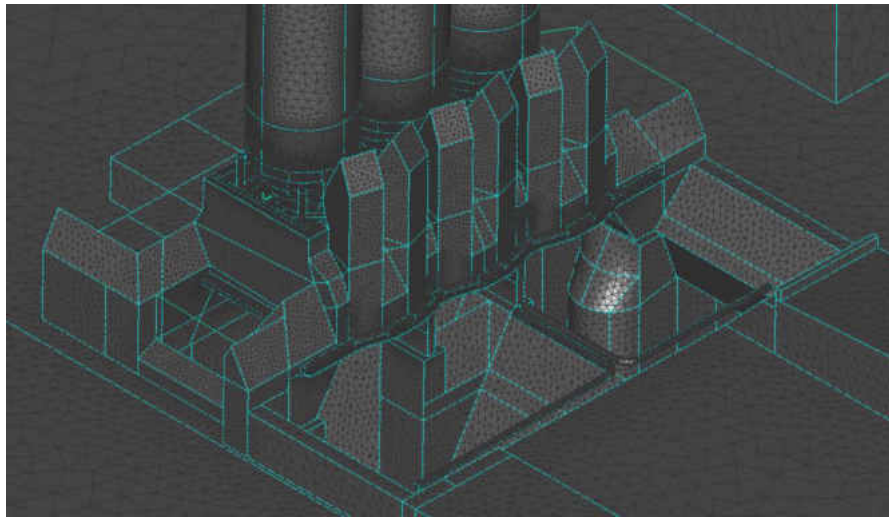


Figure 5: Full scale VAFB tetrahedral mesh.

All of the plume mitigation strategies required some form of geometry or mesh manipulation. For the air injection cases, geometry was added around the launch vehicle nozzles as a mockup of what the potential real world installation would look like. Geometry was added to the outside of the launch table structure to act as the air curtain. Air flow delivered by the air curtain is directed downward at an angle and is intended to create a barrier for the rising hydrogen plume, impeding the upward buoyant movement and blowing the plume away from the

launch vehicle. The air curtain geometry is shown in Figure 6. In addition to the air curtain geometry on the outside of the launch table structure, duct geometry was added on the periphery of the large launch table opening intended to further enhance the plume mitigation effort, see Figure 6. This geometry is of the same shape and size as the previously mentioned air curtain geometry and acts as another line of defense against the rising hydrogen plume.

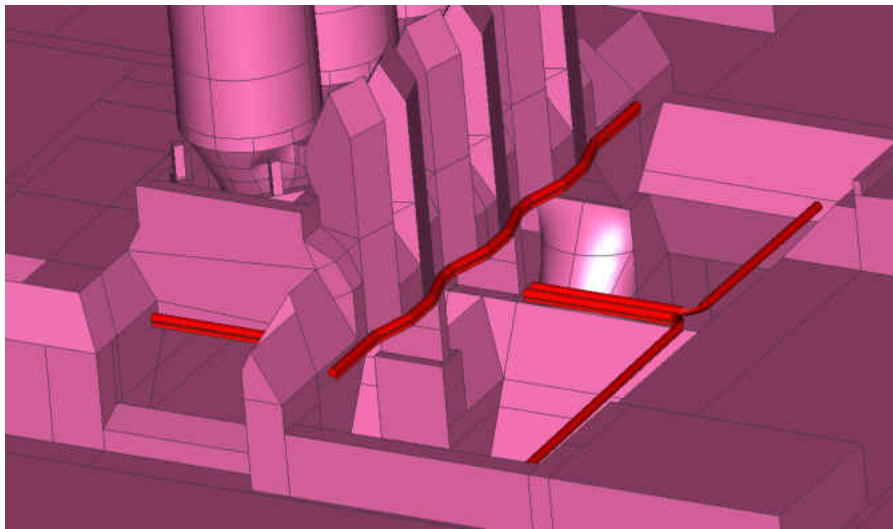


Figure 6: Air curtain geometry (shown in red).

In addition to the air injection and air curtain geometry, a “venturi” system was added to both of the flame trenches on the full scale model, Figure 2. The intent of the venturi system was to deliver a large volume of air at slower speeds to induce air movement inside of the flame trench in order to encourage the hydrogen plume to move away from the launch vehicle. Two different venturi injection angles were considered and the resulting mesh of one such angle is shown in Figure 7. For reference, the flame trench geometry without the venturi system is shown in Figure 8.

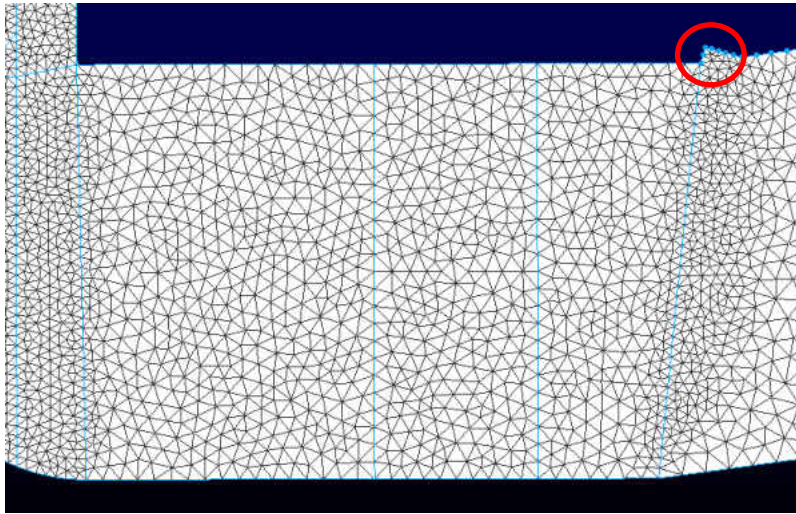


Figure 7: VAFB flame trench section with venturi system.

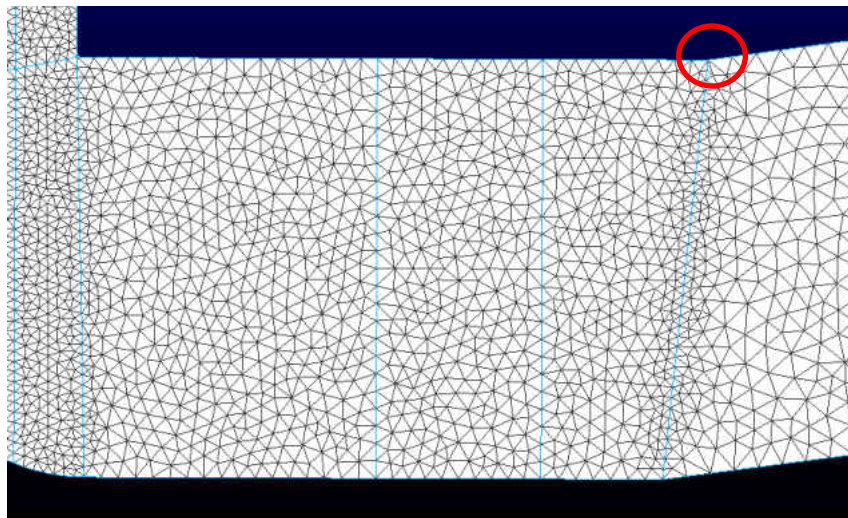


Figure 8: VAFB flame trench section without venturi system.

All of the geometry manipulation was performed in Solidworks 2010. Manipulating the geometry for the venturi system proved to be easier than the air injection and air curtain systems; an outward facing notch was added near the exit of the flame trench.

CHAPTER 3: RESULTS

As mentioned previously, a reduced VAFB model was produced to test many plume mitigation strategies and combinations. With a smaller mesh size, results could be obtained relatively quickly and incorporated into the future simulations. All of the air injection, air curtain and venturi simulations were run with several seconds added prior to the launch vehicle engine start sequence to allow the flow field created by the plume mitigation strategies to develop. The results presented here are logically separated into reduced model results and full scale results. In order to visualize the flame front created during the launch sequence of the Delta IV, an iso-surface of constant temperature was created to represent the flame boundary as it rises from the launch table. All flow rate data, for both plume mitigation and launch vehicle engines, is not included for proprietary reasons. Plume mitigation air flow rates are normalized against a “base flow rate” for presentation here.

Reduced VAFB Model

The reduced VAFB model was used to run a large number of scenarios ranging from a no injection validation case to an air injection and air curtain combination case. A total of three different air injection flow rates and equivalent air curtain flow rates were applied to the reduced model. “Equivalent” air curtain flow rates were determined by calculating the air curtain flow rate required to achieve the same velocity observed in the air injection cases. In addition, two different air injection angles were explored over the course of the reduced model study. In all cases it was assumed that the desired air flow rate was supplied instantaneously. All of the different combinations completed are summarized in Table 1.

Table 1: Summary of reduced model cases completed.

	Air Injection				Air Curtain		
	0.5x base flow rate	Base flow rate	Base inclination angle	2.5x base inclination angle	0.5x base flow rate	Base flow rate	1.6x base flow rate
Case 1	-	-	-	-	-	-	-
Case 2	X	-	X	-	-	-	-
Case 3	X	-	-	X	-	-	-
Case 4	-	X	X	-	-	-	-
Case 5	-	X	X	-	X	-	-
Case 6	-	X	X	-	-	X	-
Case 7	-	X	X	-	-	-	X
Case 8	-	X	-	X	-	-	-

Several different ideas needed to be considered when determining what the most effective plume mitigation strategy would be. Does air injection angle matter? Is an air curtain effective against the rising hydrogen plume? First, a base air flow rate was chosen and any future studies would be based off of the results from that simulation. As shown in Table 1, the effect of the air injection and air curtain systems were determined by both reducing and increasing the base air flow rate by as much as a factor of 1.6.

Air Injection Inclination Comparison

The first question addressed was if the angle of the air injection nozzles had any effect on hydrogen plume mitigation. A mesh with a relatively shallow base inclination angle was chosen (relative to the vertical) and another model was made with an injection angle increased by a factor of 2.5. The air injector geometry and flow rate was held constant between the two different injection angles. The flow rate was chosen to be half that of the base flow rate. The air injection inclination comparison covers Case 2 and Case 3 in Table 1.

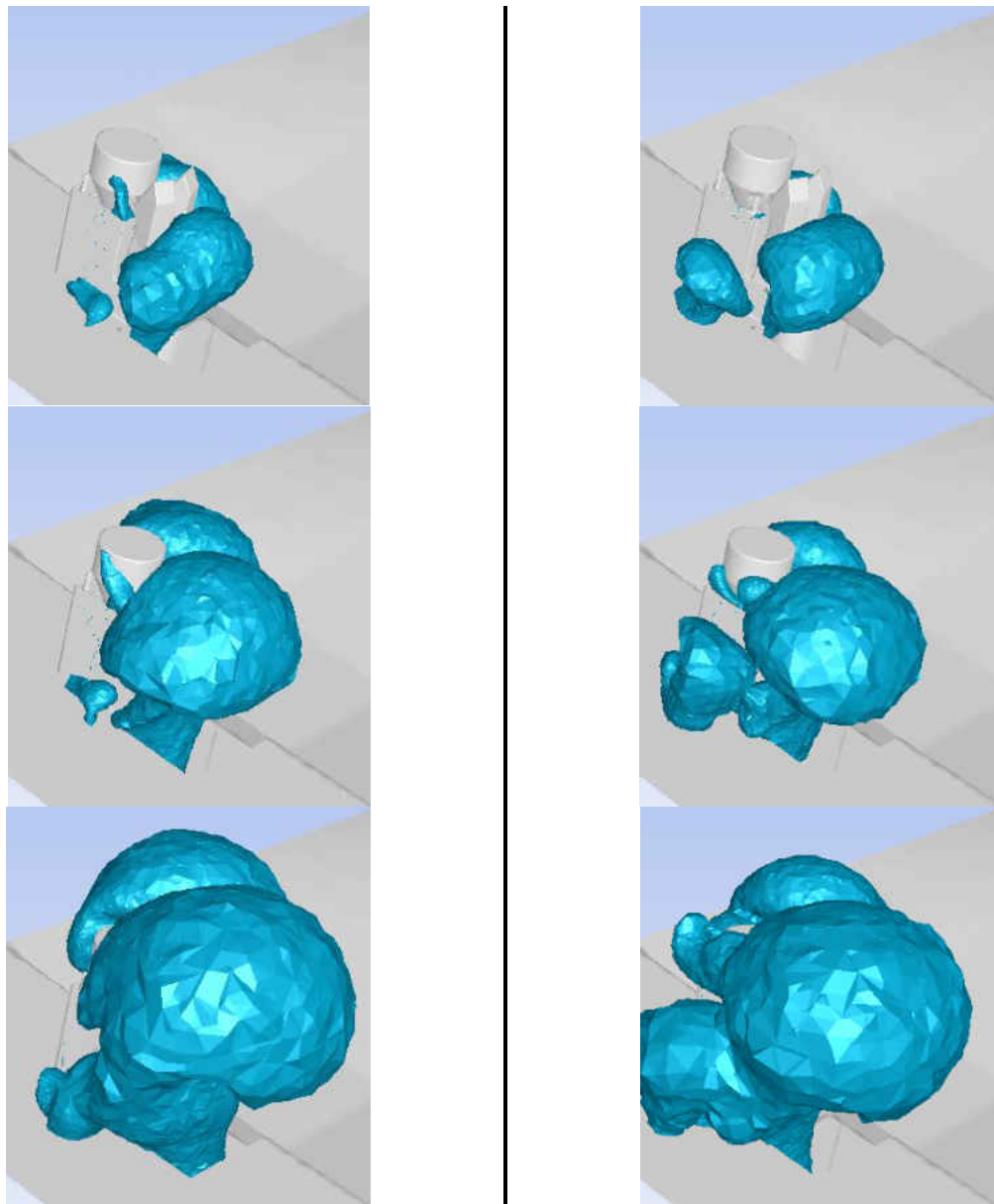


Figure 9: Hydrogen plume rise for the base inclination angle (left) and 2.5x base inclination angle (right) air injection simulations.

The hydrogen plume rise for both the base air injection inclination angle and the increased air injection inclination angle is shown in Figure 9. The screenshots are taken at the same time intervals for both cases and time increases down each column. The large plume bulb produced in the foreground of the first frames in Figure 9 is due to the lack of plume mitigation around launch table opening (see Figure 4 and Figure 5) and is only slightly affected by the air injection system. Initially, it can be seen that the base inclination angle allows a portion of the flame front to emerge from the engine section before the increased injection angle does the same. The behavior changes as time progresses; the second and third frames of Figure 9 show that the increased air injection angle allows a significant portion of the hydrogen plume to rise through the engine section while the base injection angle does not. The flame front rises vertically so it makes sense that the smaller injection angle (closer to the vertical direction) is more effective against the flame rise. An approximate relationship to describe the required injection air velocity to suppress a given hydrogen plume has been developed and was shown to agree with the 0.5x base flow simulations. Due to the more desirable performance of the base inclination angle, all of the models were made using that orientation.

Air Injection Flow Rate Comparison

The next series of simulations completed were aimed at determining the effect different flow rates had on the hydrogen plume rise. Two flow rates were chosen: a base flow rate and 0.5x base flow rate. According to the air injection orientation simulations, the base inclination angle was the most successful so it was used on both models. A summary of the results are shown at three different time intervals in Figure 10 below. Figure 10 depicts Cases 2 and 4 from Table 1. The base flow rate noticeably outperforms the 0.5x base flow rate case, which is

expected. The second and third frames of Figure 10 show that the base flow rate is successful at nearly eliminating the plume rise coming from the engine section while, as also observed in Figure 9 (left), the 0.5x base flow rate case allows a flame to rise upward. It is important to note that while the flame emanating from the engine section is greatly reduced with the base flow rate, the flame “bulb” exiting through the large launch table opening grows in size when compared to the 0.5x base flow rate case. This means that the flame suppressed around the engine section is essentially pushed down and out of the large launch table opening only to rise towards the launch vehicle. The air curtain system is intended to remedy this problem and push the flame away from the launch pad. Based on the results of these simulations, the base flow rate for the air injection systems used in the upcoming air curtain simulations was the same base flow rate used in Figure 10 (right).

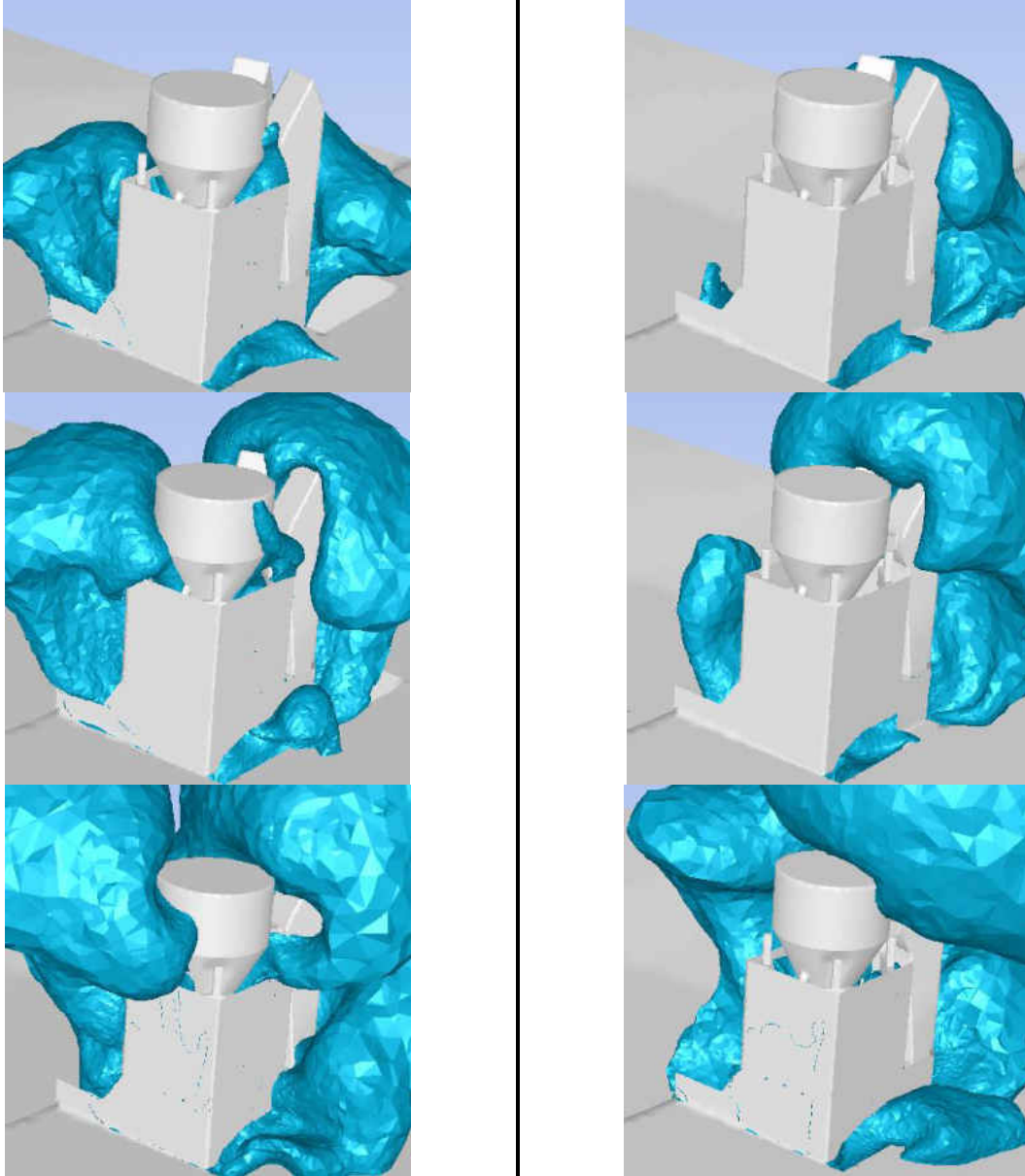


Figure 10: Hydrogen plume rise for 0.5x base flow rate (left) and base flow rate (right) air injection simulations.

Air Curtain Flow Rate Determination

The flame front rising from the engine section is effectively controlled with air injection alone, as seen in Figure 10 above. However, the large plume bulb created as a result of air injection is a concern that needed to be addressed. An air curtain system, installed around the launch table periphery, is a possible solution to this problem. Figure 11 depicts the flame boundary progression as time increases for a 0.5x base flow rate air curtain, a base flow rate air curtain, and a 1.6x base flow rate air curtain. It should be noted that all of the cases presented in Figure 11 include a base flow rate air injection system. Figure 11 encompasses cases 5-7 in Table 1. Each row of frames in Figure 11 is taken at the exact same time into the launch sequence. In addition, each row is separated by the same amount of time.

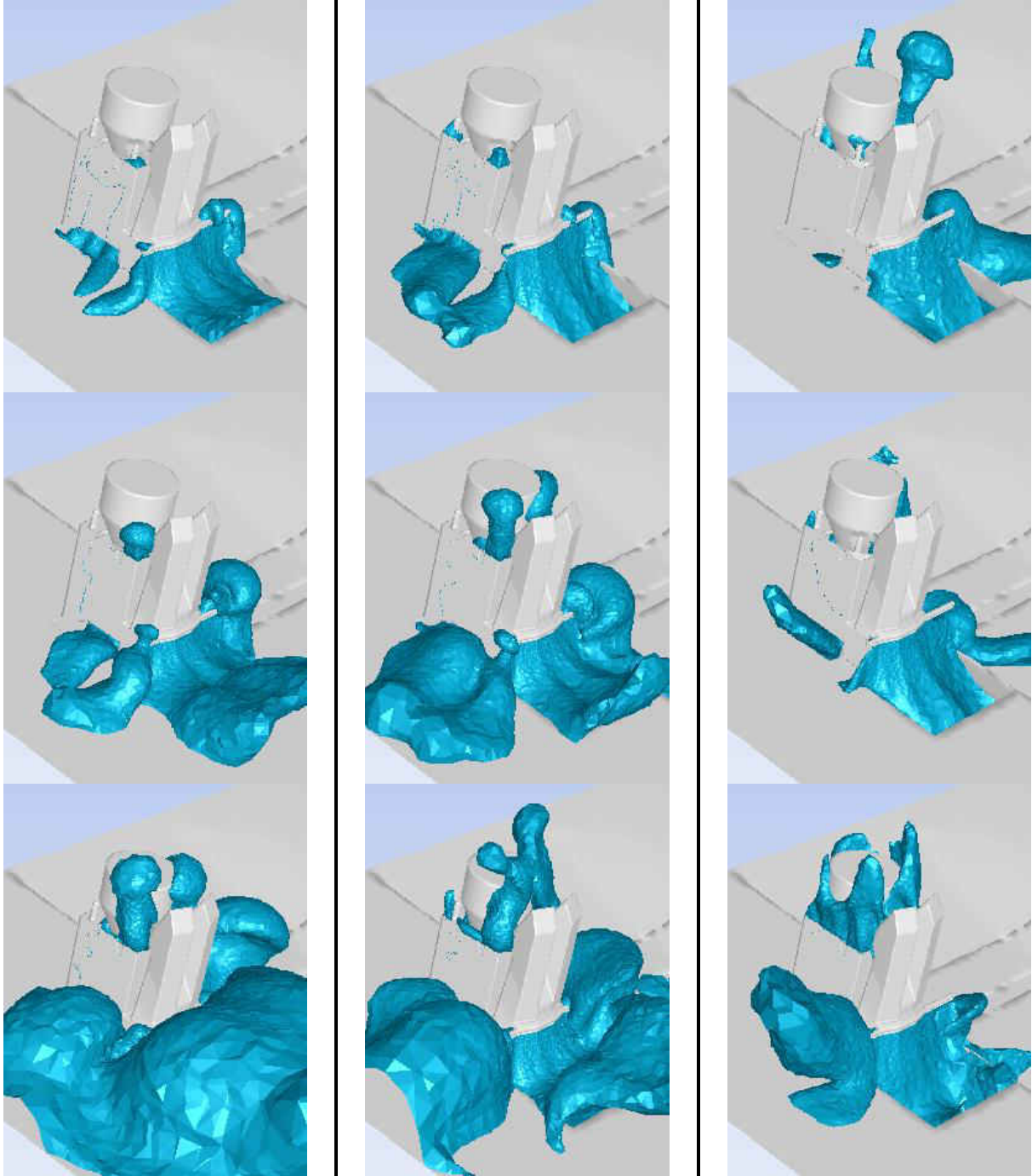


Figure 11: Hydrogen plume rise for 0.5x base flow rate (left), base flow rate (center), and 1.6x base flow rate (right) air curtain simulations.

As seen in Figure 11, the air curtain system has a large impact on the hydrogen plume behavior. In the first few frames of Figure 11, the flame boundary shapes are very similar. Once the engine start sequence ramps up and a large amount of hydrogen is introduced into the launch table, the plume behavior starts to change. The 0.5x base flow rate air curtain starts out promising and the flame boundary is pushed away from the launch vehicle. However, the 0.5x base flow rate air curtain is ultimately overpowered by the rising plume. The base flow rate case offered an improvement over the 0.5x base flow rate case, as expected. In the last frame of Figure 11 (center), it can be seen that the base flow rate offers a more robust solution due to the fact that the mitigation system was not overwhelmed to the same degree as the 0.5x base flow rate case. The most effective flow rate of the three air curtain cases was the 1.6x base flow rate case, which is not entirely surprising; a larger flow rate through the same geometry translates to a larger air velocity. The difference is quite drastic when the final frames of the 0.5x base flow rate (Figure 11, left) and the 1.6x base flow rate (Figure 11, right) are compared. The size of the flame boundary is greatly reduced in the 1.6x base flow rate case. It's interesting to note that as the air curtain flow rate is increased, the presence of the plume escaping from the engine section (in the vicinity of the launch vehicle) increases. This trend is most easily seen in the final frames of each case in Figure 11. This behavior occurs because as the air curtain flow rate increases, the pressure inside of the engine section increases relative to the ambient. As a result, it is easier for the plume to move upward against the air injection system. Despite this, the 1.6x base flow rate air curtain case clearly outperforms the 0.5x and base flow rate cases.

Reduced VAFB Model Conclusions

In addition to all of the plume mitigation simulations discussed above, a model was run with no mitigation whatsoever. This model was intended to provide a point of comparison for the mitigation models as well as a test to see if the launch sequence is properly modeled. One main characteristic is “launch table aspiration”. This occurs when the bulk flow exiting from the launch vehicle is large enough to create a suction effect and pull a portion of the plume back into the launch table. Figure 12 below shows how the plume is cut off by the suction effect. At this point any plume mitigation air flow is overpowered by the large mass flow rate from the launch vehicle.

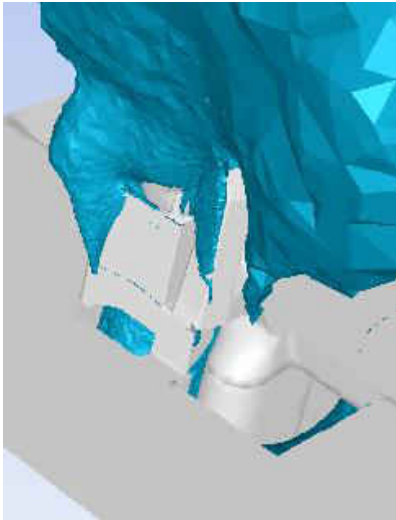


Figure 12: Launch table aspiration.

The impact of adding plume mitigation to the Delta IV launch pad can be readily seen in Figure 13, which shows the base air flow rate injection with a 1.6x base flow rate air curtain alongside a simulation with no injection. As with the other figures, both represent the hydrogen plume at the same time intervals.

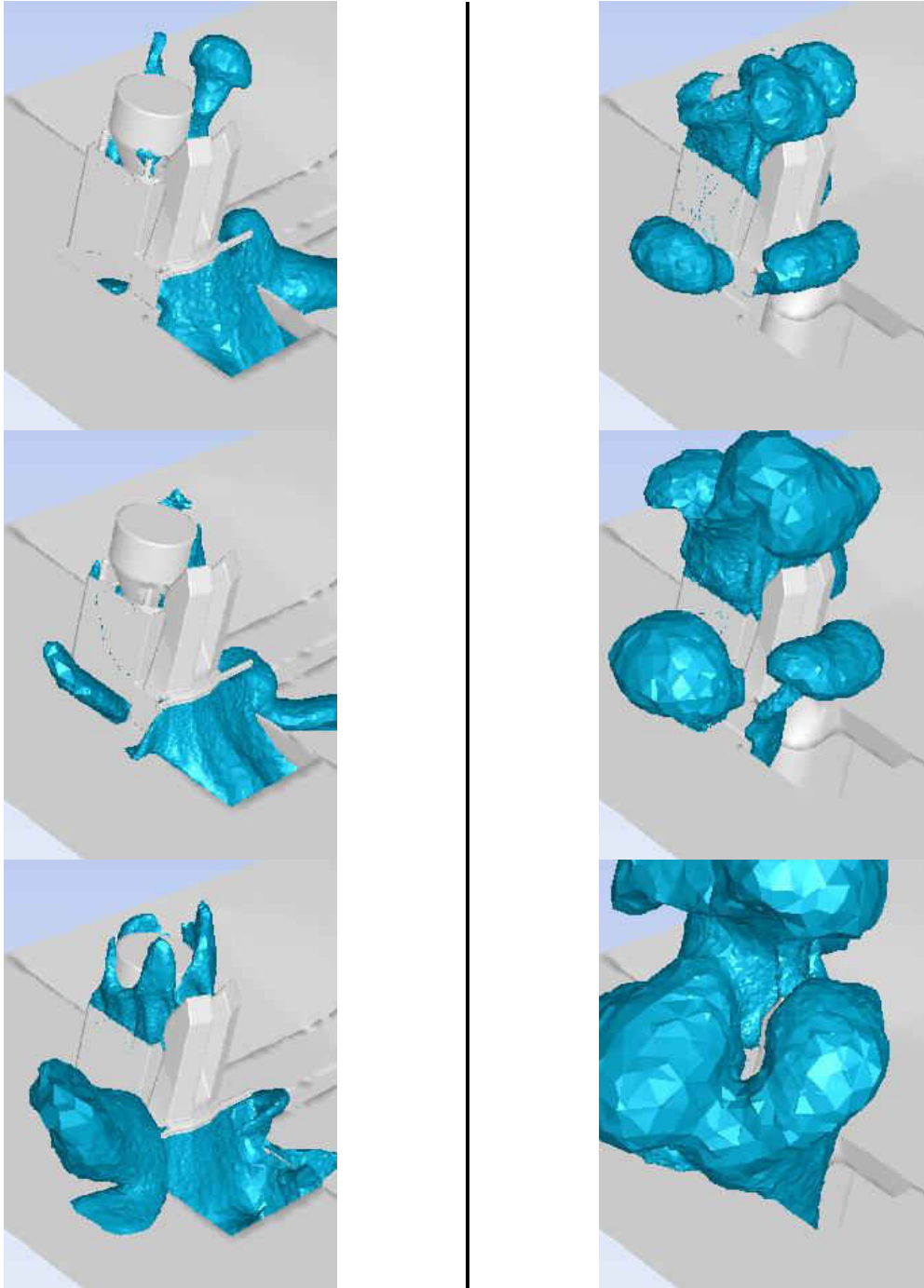


Figure 13: Hydrogen plume rise for base air flow rate injection with 1.6x base flow rate air curtain (left) and no injection (right).

The first frame of Figure 13 already shows a big improvement in plume size in the immediate vicinity of the launch vehicle. The only significant flame presence is on the far side of the frame and is negligible when compared to the no injection case. As time progresses, the air curtain successfully does its job and prevents any flame from rising out of the large launch table opening. As mentioned before, the increased back pressure inside the launch table in the air curtain and air injection case results in some flame emerging from the engine section as seen in the final frame of Figure 13. The final frames of Figure 13 tell the entire story: adding an air injection and air curtain system dramatically reduce the plume size produced in the reduced model. The next step was to apply these mitigation strategies and flow rates to the full model and see how well they scale up.

Full Scale VAFB Model

Based on the reduced model results, it was decided that the 0.5x base flow rate air injection was not effective enough to warrant a full scale model run. Thus, the base flow rate and 1.6x base flow rate air injection scenarios were used on the full scale model. Although the 1.6x base flow rate air curtain was the most successful, the volumetric flow rate requirement for that case on the full scale model was deemed too large to produce in practice. Therefore the base flow rate air curtain was the only scenario considered. A total of 5 different cases were run with different combinations of plume mitigation strategies in addition to 1 validation case with no mitigation present. Again, the flame boundary for each case was visualized by plotting an iso-surface of constant temperature to emulate the flame boundary observed during liftoff. Since the plume mitigation strategies are overpowered by launch table aspiration and required very long run times, all of the cases were run at least up to aspiration but not necessarily for the entire

launch timeline. Again, at the start of the simulation, the air injection, air curtain, and venturi systems are assumed to deliver the desired flow rate instantaneously. The launch timeline was extended by several seconds to allow the flow field induced by the plume mitigation system to approach steady state prior to launch vehicle engine ignition. Table 2 shows a summary of the combinations of plume mitigation analyzed.

Table 2: Summary of the full scale cases analyzed.

	Air Injection (Base Flow Rate)	Air Injection (1.6x Base Flow Rate)	Air Curtain	Venturi
Case 1	-	X	-	-
Case 2	X	-	X	-
Case 3	X	-	-	X
Case 4	X	-	X	X
Case 5	-	-	-	-

1.6x Base Flow Rate Air Injection

One of the first mitigation strategies investigated for the full scale model was a 1.6x base flow rate air injection scenario, specifically Case 1 in Table 2 above. This case was not considered in the reduced model but it was of interest to see what advantages an increased flow rate over the base flow rate offered. As mentioned before, all of the full scale models use the base inclination air injection geometry discussed in the previous section. Figure 14 shows the hydrogen plume progression as a function of time at four different intervals separated by the same amount of time. The first two frames of Figure 14 show that the 1.6x base flow rate air injection seems to be suppressing any flame from rising out of the engine section near the launch vehicle. Unfortunately, a large plume was produced from the launch table opening in front of the

launch vehicle and the view was obscured. The hydrogen plume's effect on the launch vehicle is most easily seen by contour plots of surface temperatures, included in Figure 15 and Figure 16. The plume exiting from the launch table opening rose up next to the launch vehicle and resulted in elevated surface temperatures reaching nearly halfway up the vehicle body. Note that Figure 15 shows a region of high temperature near the bottom of the launch structure. This case was run before the radiation model was implemented and this resulted in regions of increased temperature. Figure 16 shows temperature contour plots for the opposite side of the launch vehicle presented in Figure 15. No elevated temperatures can be seen on this side of the launch vehicle which means that the 1.6x base flow rate air injection is enough to suppress any flame from rising through the engine section of the launch table. This also means that the elevated surface temperatures shown in the last two frames of Figure 15 are a direct result of the large plume bulb (see Figure 14) rising near the launch vehicle. A logical conclusion to be drawn from Figure 15 and Figure 16 is that inclusion of an air curtain system with the 1.6x base flow rate air injection system has the potential to eliminate the entire hydrogen plume. Unfortunately, it turns out that introducing more air flow into the launch table results in an increased back pressure and a loss in plume suppression effectiveness, which will be discussed in a future section.

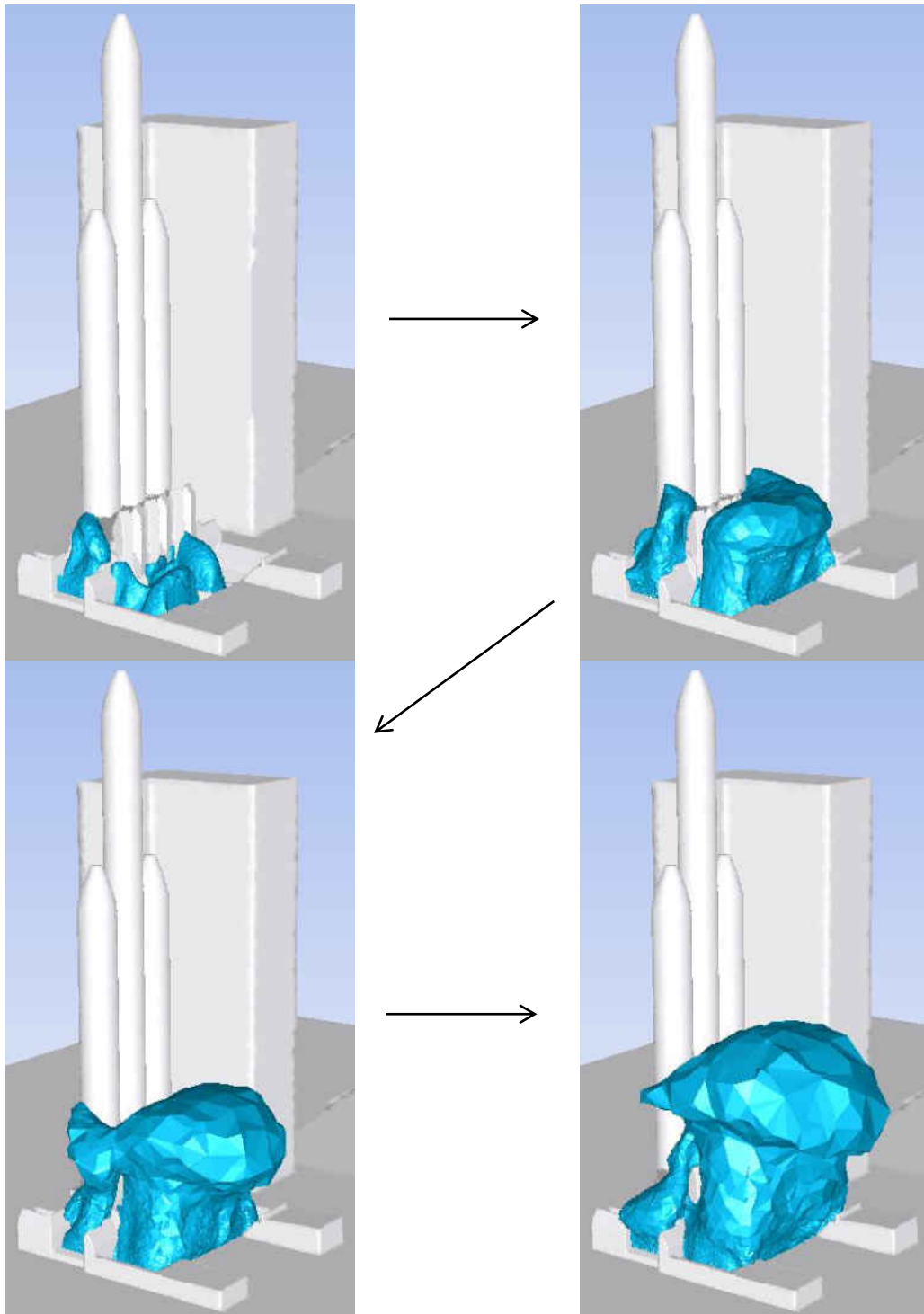


Figure 14: Hydrogen plume rise for the 1.6x base air injection case.

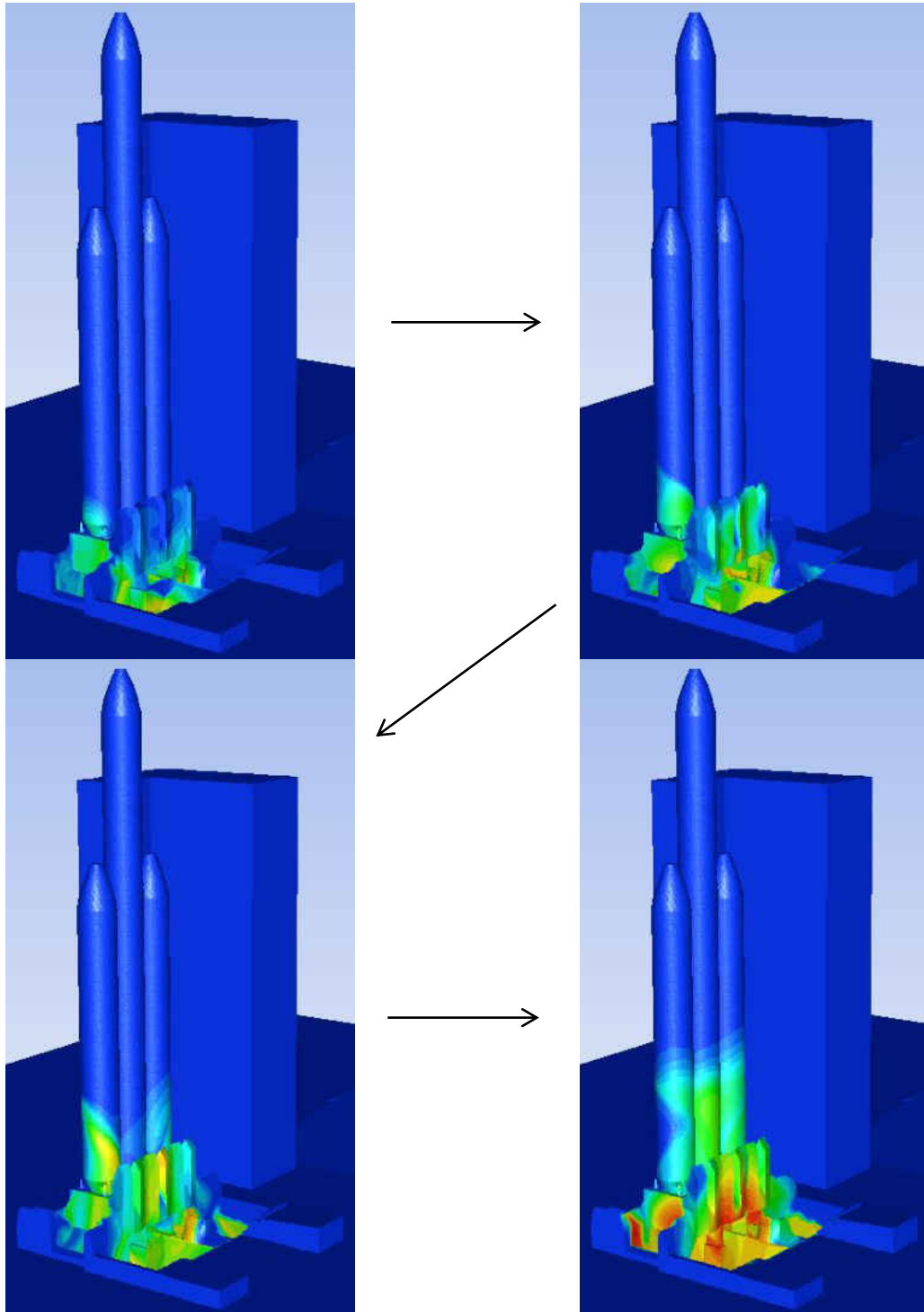


Figure 15: Surface temperature contour plots for the 1.6x base air flow rate injection case.

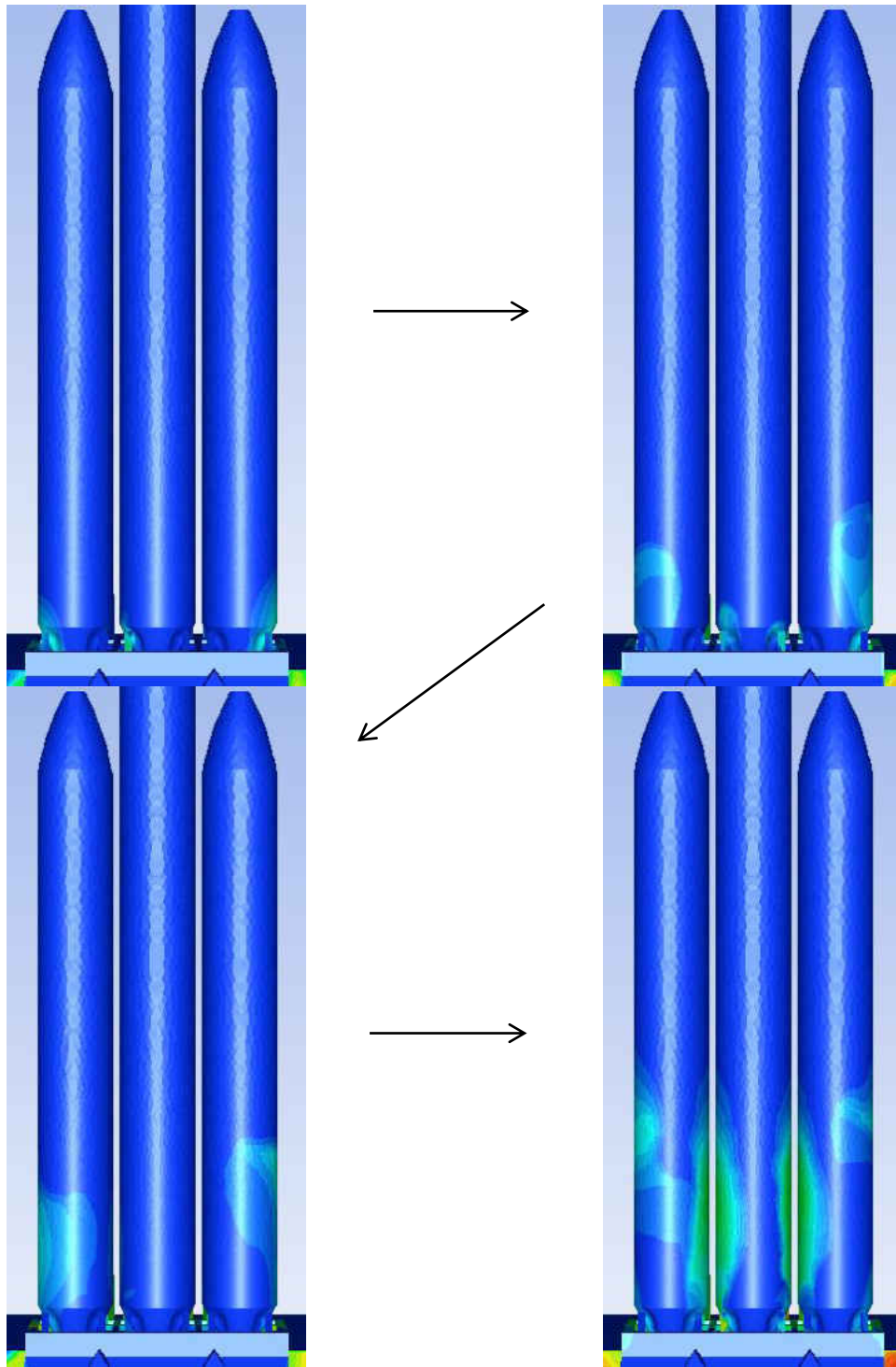


Figure 16: Additional surface temperature contour plots for the 1.6x base air injection case.

Base Flow Rate Air Injection and Air Curtain

Case 2 in Table 2 is the full scale equivalent of Case 6 in Table 1 whose results were presented in Figure 11. The full scale results are shown below in Figure 17. The first frame of Figure 17 shows a promising plume shape: the air injection system has suppressed any flame from rising near the launch vehicle up to this point and the air curtain system is pushing the flame away from the launch table. As time progresses and more unreacted hydrogen is introduced, the mitigation systems again become overwhelmed. The final frame of Figure 17 shows the size of the plume bulb escaping from the air curtain system. As with the reduced models, the air injection and air curtain systems caused an increase in pressure inside of the launch table and thus flame was pushed upwards and allowed to escape the engine section. This behavior is most easily seen in frames 2-4 of Figure 17. Of course, the flame iso-surface plots are only part of the story. The insulation charring is a result of elevated launch vehicle surface temperatures so it is interesting to plot how that temperature changes as time progresses. Surface temperature contour plots for the same time intervals shown in Figure 17 are shown in Figure 18. The temperature scale ranges from blue (lowest temperature) to red (highest temperature). Note that all of the walls in every model are assumed adiabatic so Figure 18 represents a worst case scenario. In the final frame of Figure 18, the high temperature region reaches nearly half way up the launch vehicle. Additionally, temperature contour plots for the back side of the launch vehicle not shown in Figure 18 are provided in Figure 19.

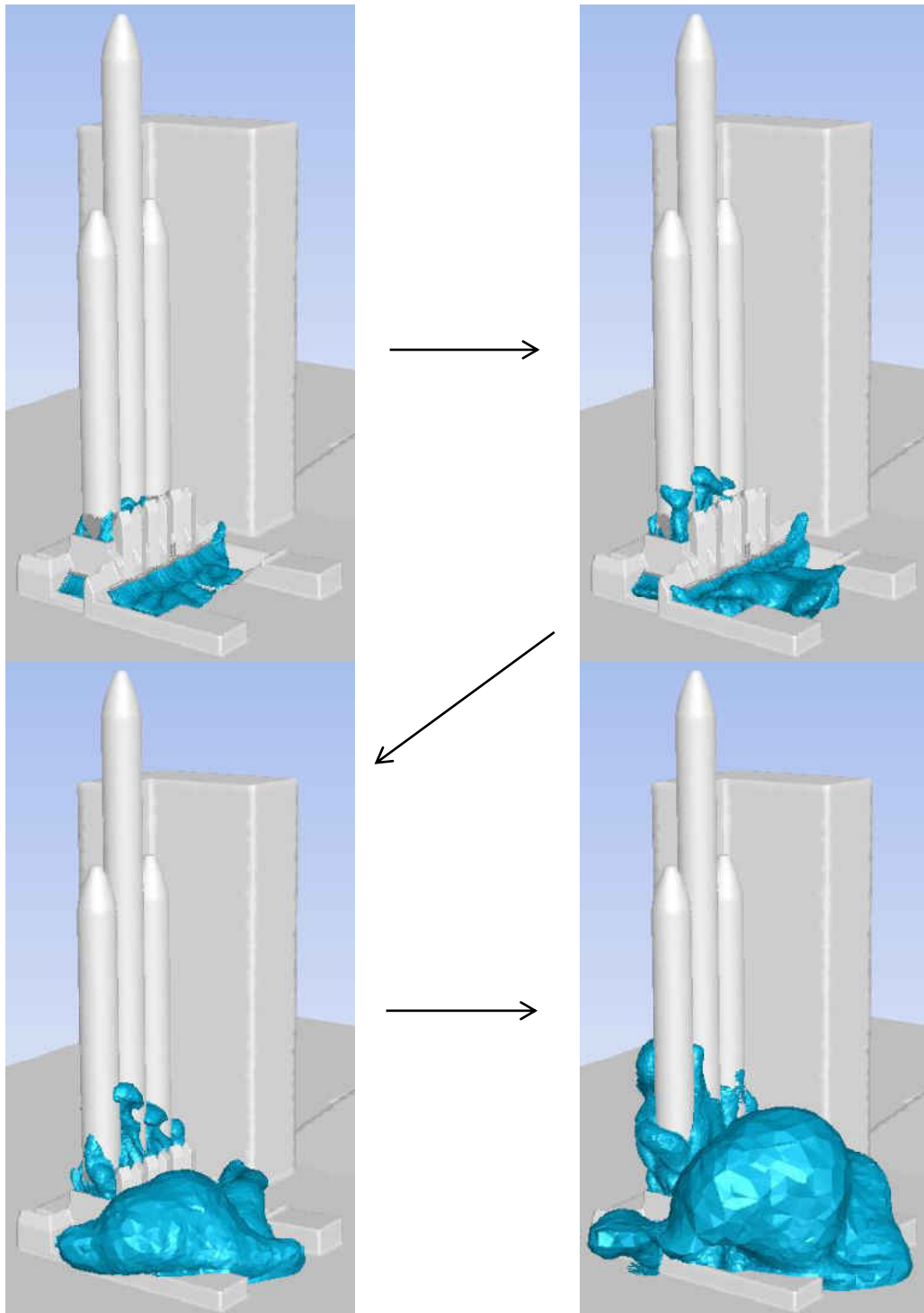


Figure 17: Hydrogen plume rise for the base air injection flow rate and base air curtain flow rates.

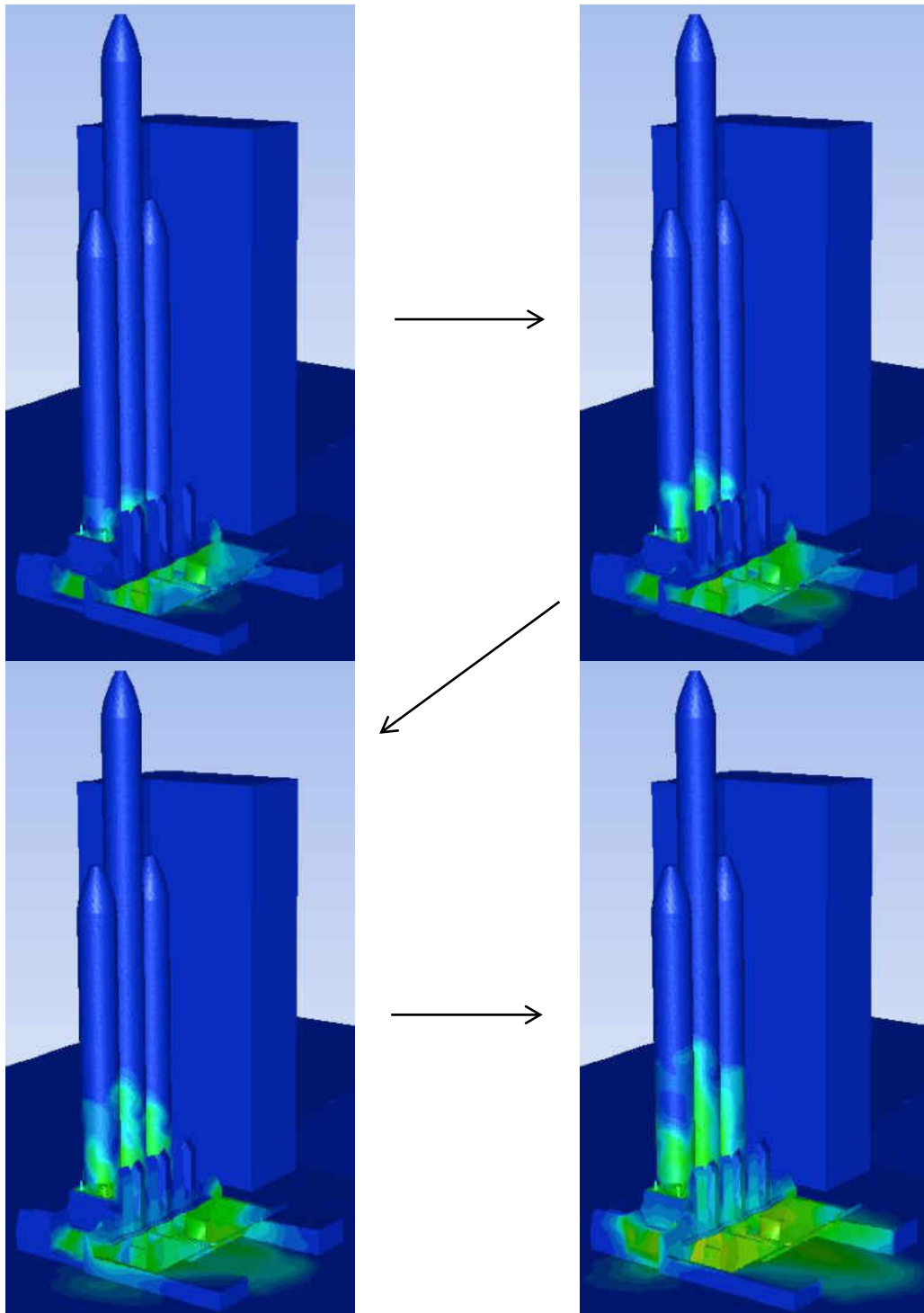


Figure 18: Surface temperature contour plots for the base air injection and base air curtain flow rates.

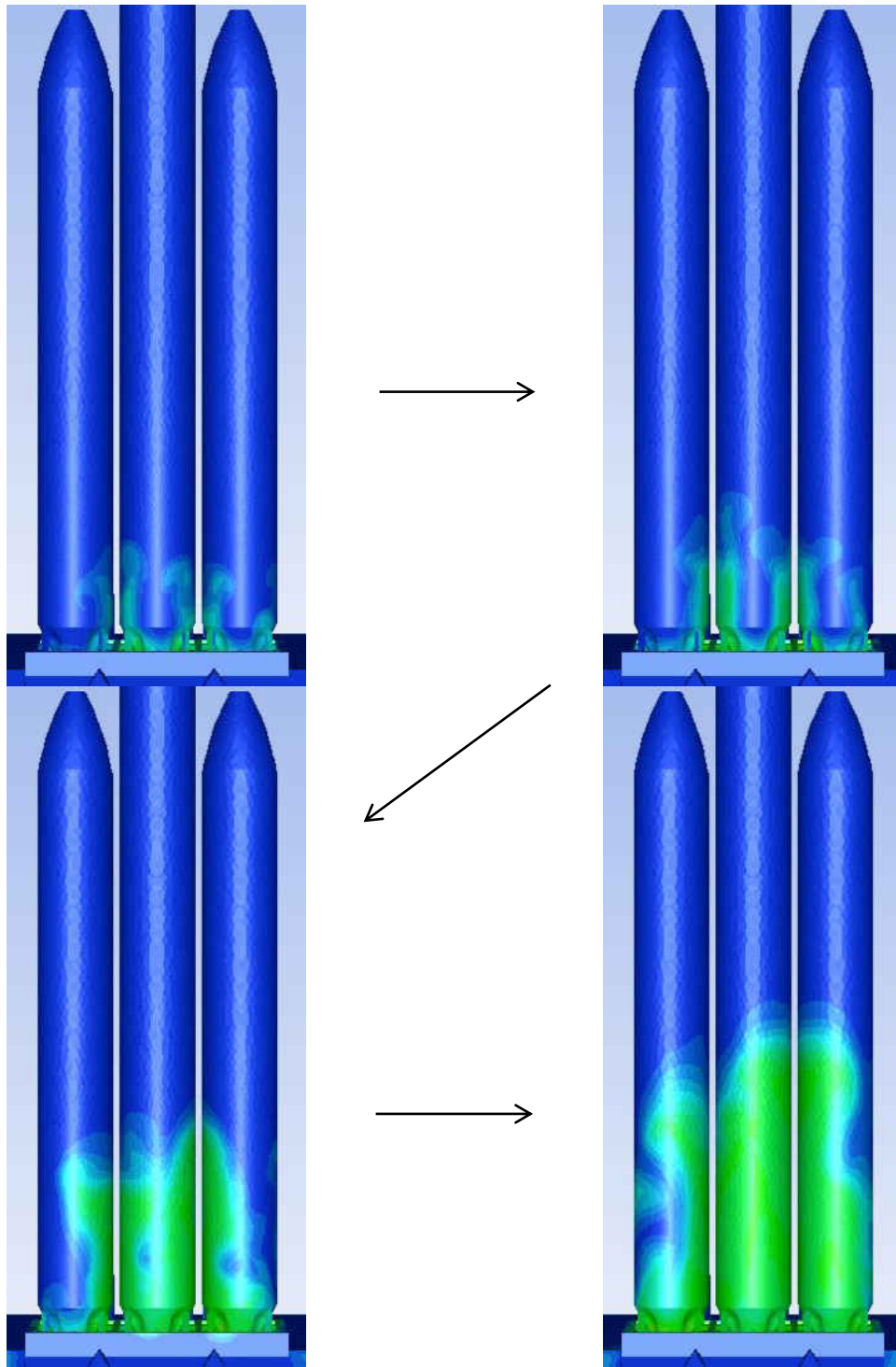


Figure 19: Additional surface temperature contour plots for the base air injection and base air curtain flow rates.

Base Flow Rate Air Injection and Venturi

The base flow rate air injection and venturi case is denoted by Case 3 in Table 2. The venturi system outlet was much larger than the air injection and air curtain systems and thus required a very large volumetric flow rate however the air was delivered at a much lower velocity. Several steady state analyses were done on the venturi configuration alone, mainly focused on venturi angle, in order to quantify effect the system had on air speed at the launch table. It was found that with no injection, velocities at the engine section saw a 10% increase when a shallow venturi injection angle was used. In other words, pointing the venturi system in line with the flame trench is the most effective direction. The results for the base flow rate air injection and venturi case are shown below in Figure 20, Figure 21, and Figure 22. Similar to the 1.6x base air injection case (see Figure 14), a large flame exits from the launch table opening (see the foreground of Figure 20) and rises upward to the launch vehicle. The surface temperature contour plots (Figure 21) show that the front of the vehicle is subject to an elevated temperature and there is a possibility that the protective insulation would be charred. The surface temperature contours on the opposite side of the launch vehicle (Figure 22) reveal something interesting: that side of the vehicle is nearly untouched by the rising plume. It appears that the addition of the venturi system to the base flow rate air injection system has a positive effect on the hydrogen plume rise behavior. Perhaps the addition of the air curtain system will further improve the plume situation on the side of the launch vehicle shown in Figure 20 and Figure 21.

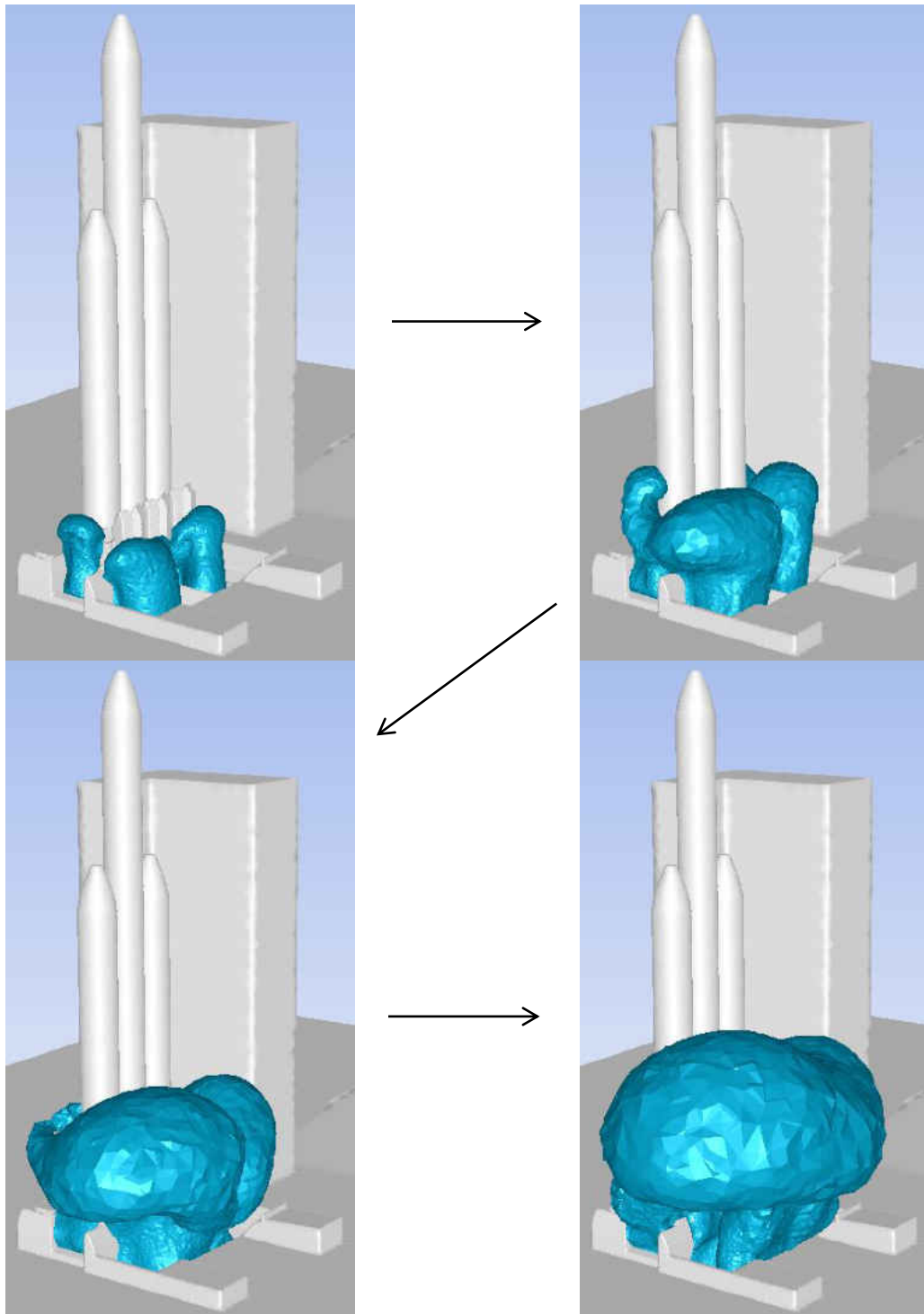


Figure 20: Hydrogen plume rise for the base air injection and venturi case.

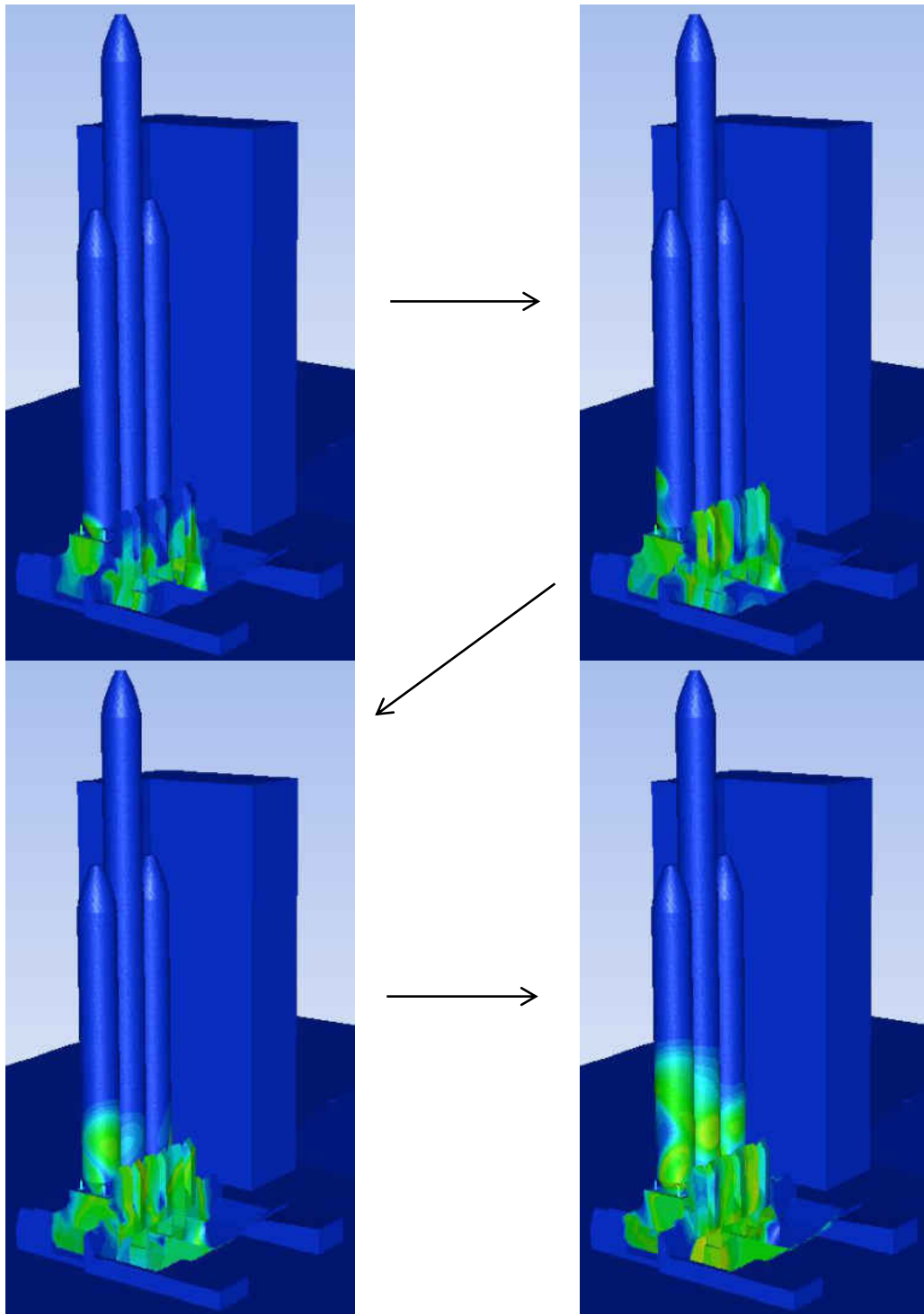


Figure 21: Surface temperature contour plots for the base air injection and venturi case.

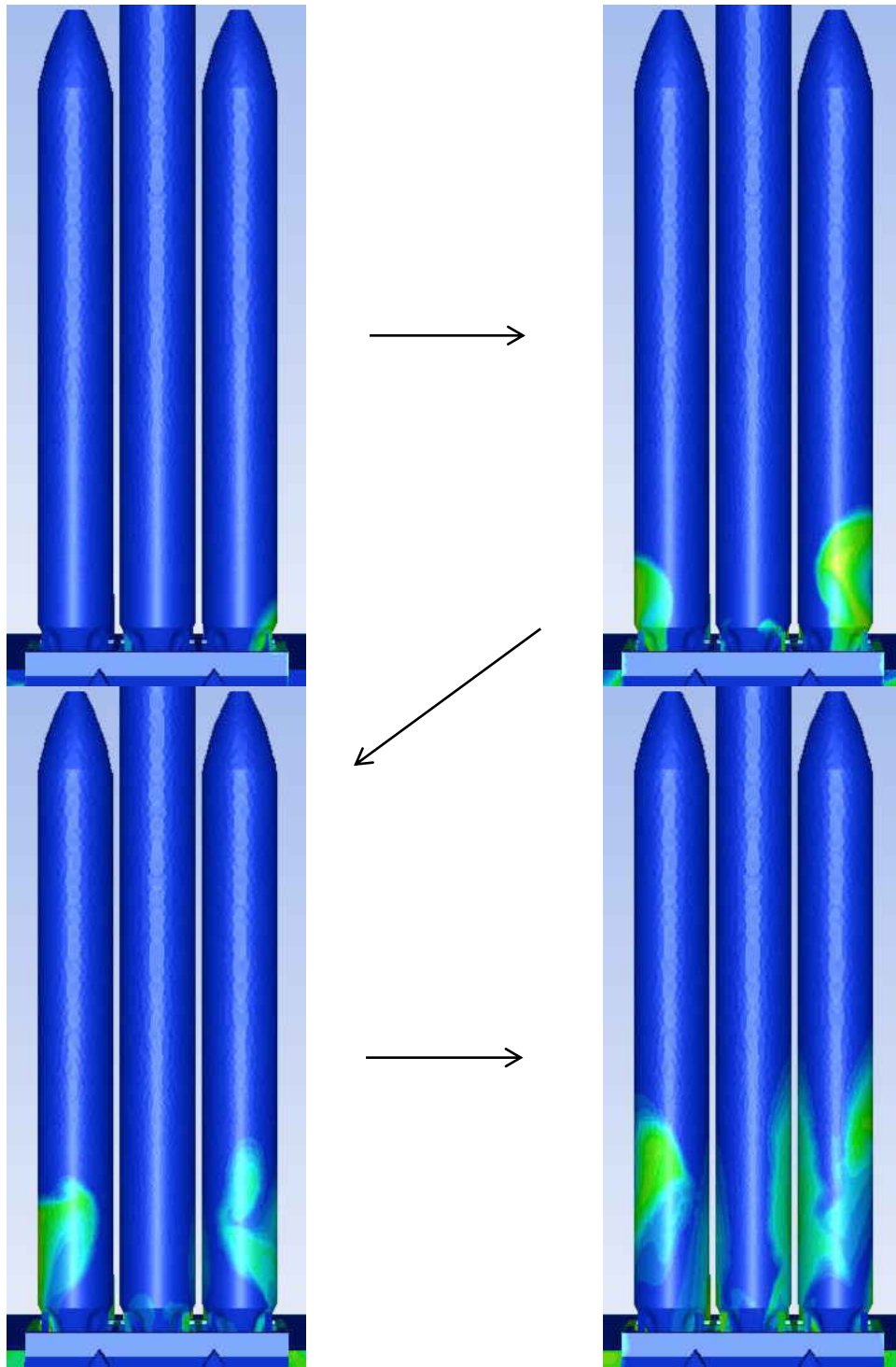


Figure 22: Additional surface temperature contour plots for the base air injection and venturi case.

Base Flow Rate Air Injection, Air Curtain and Venturi

The final combination of plume mitigation strategies considered was Case 4 in Table 2. In this case, the venturi system was added to a base air flow rate air injection and air curtain setup. Essentially Case 4 is Case 2 with a venturi system, which has been discussed previously (see Figure 7). The venturi system delivers a large amount of air at a lower velocity and is intended to induce air flow inside of the VAFB flame trench. The system was installed near the end of the flame trench and only spanned the roof of the trench. When the venturi system is used in conjunction with the air injection and air curtain systems it appears that venturi system does not significantly help the plume problem. Notice that the results shown in Figure 23 through Figure 25 are very similar to the results in Figure 17 through Figure 19. Elevated temperatures are observed on the launch vehicle (Figure 24 and Figure 25) and a large plume bulb escapes past the air curtain system (Figure 23, last two frames).

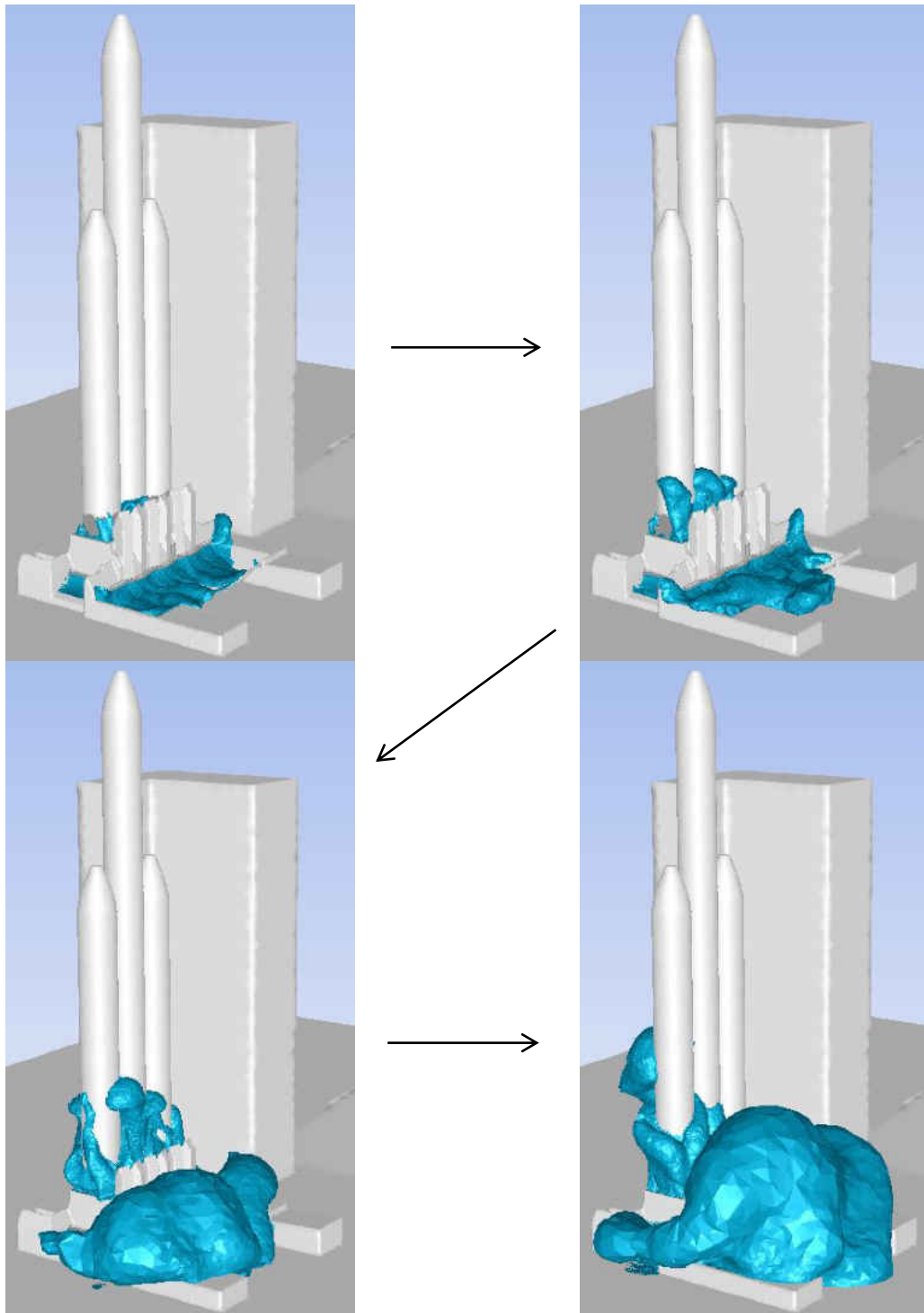


Figure 23: Hydrogen plume rise for the base flow rate air injection, curtain and venturi case.

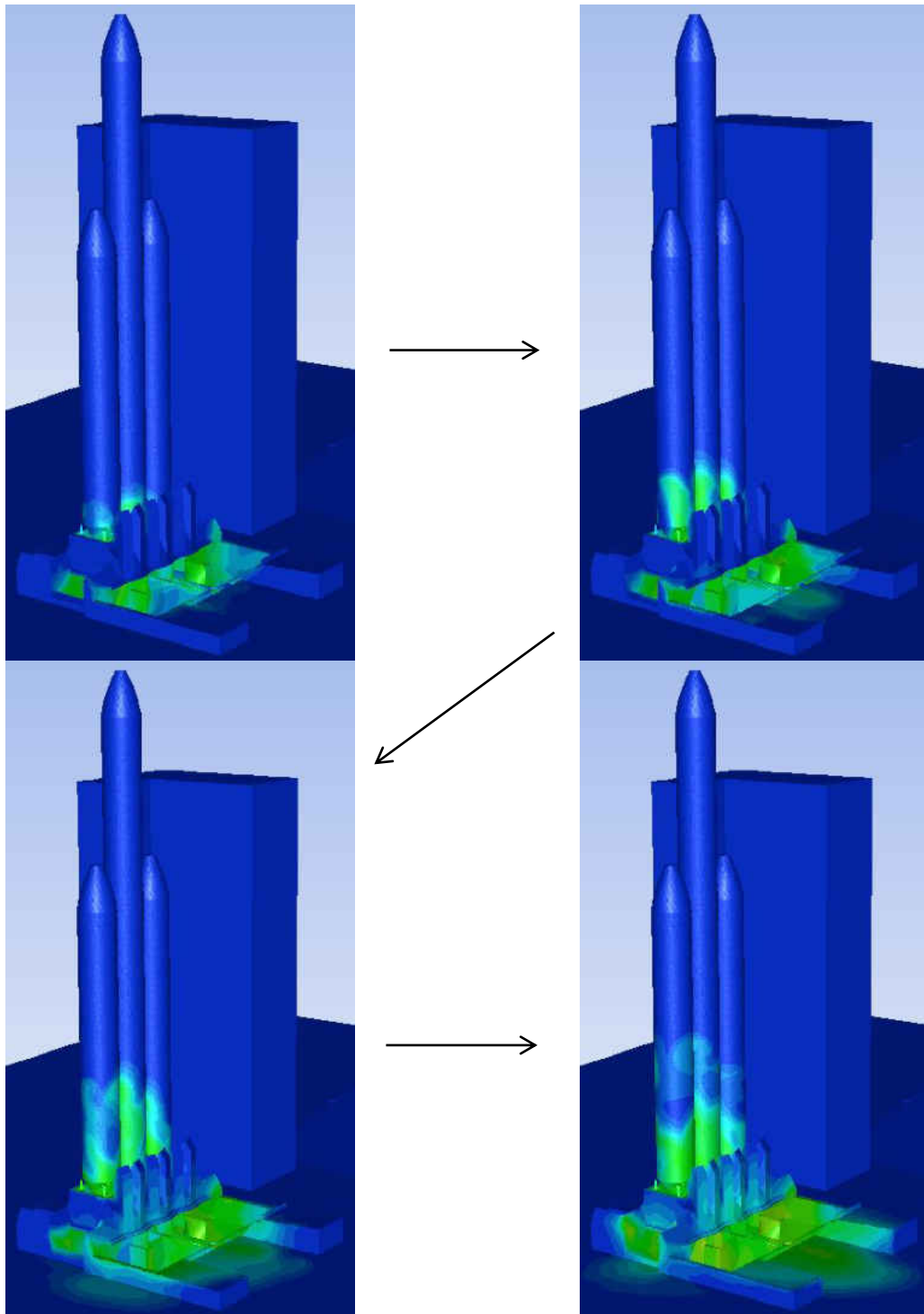


Figure 24: Surface temperature contour plots for the base flow rate air injection, curtain and venturi case.

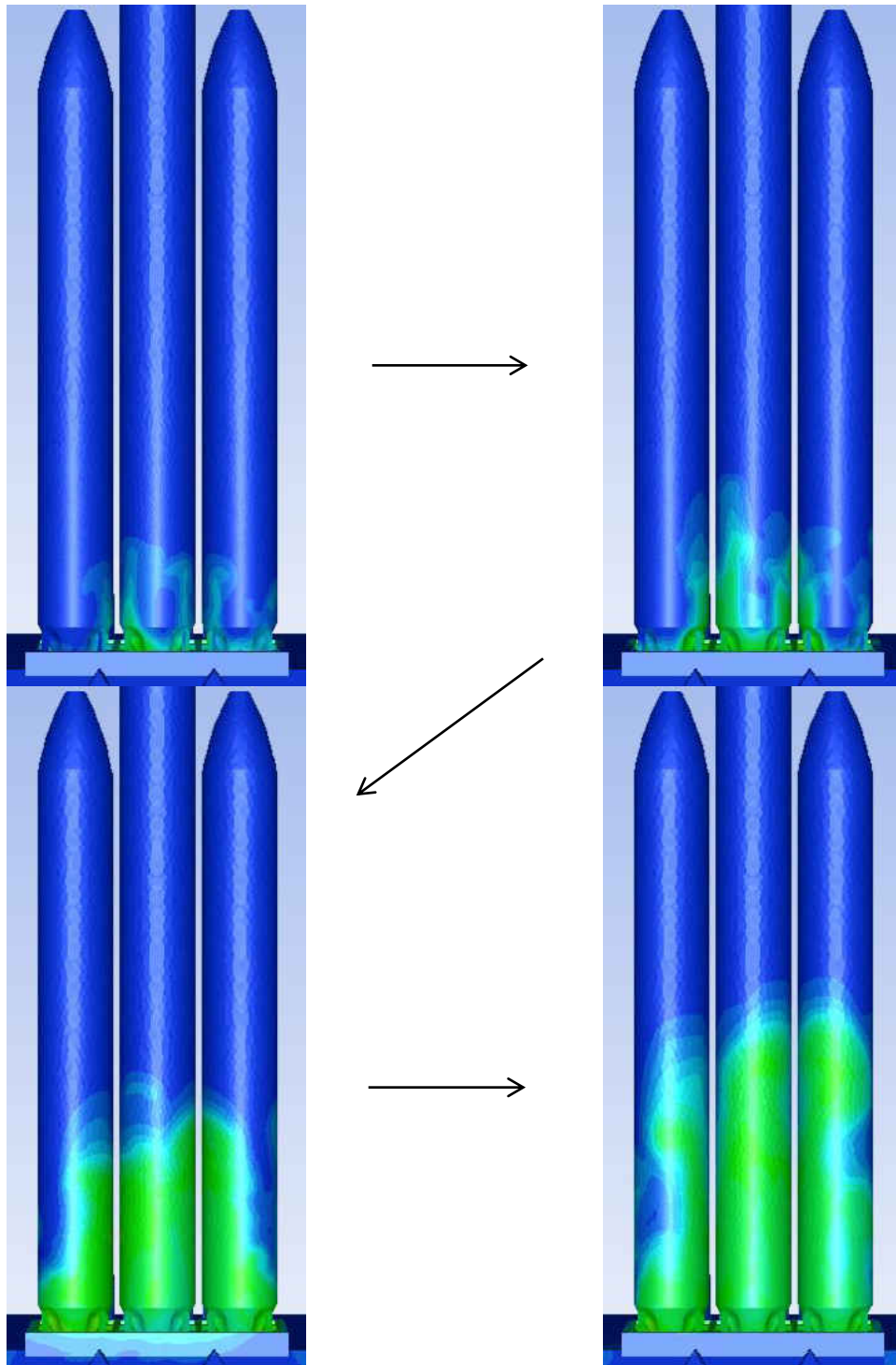


Figure 25: Additional surface temperature contour plots for the base flow rate air injection, curtain and venturi case

Case Comparison with No Mitigation Present

The extent to which the plume mitigation procedures improve the hydrogen plume problem can easily be seen by just examining the flame rise resulting from the no mitigation case alone (Figure 26). Note that the snapshots were taken at the same time into the engine start sequence as the other snapshots presented here. Even in the first frame, a significant flame emerged from the engine section of the launch table. By the final frame of Figure 26, the entire bottom half of the launch vehicle was engulfed by the rising hydrogen plume. The surface temperature contour plots (Figure 27) show that an extensive amount of the launch vehicle surface is subject to high temperatures during the launch sequence. As the flame rises, the affected areas of the launch vehicle grow larger. The only time the increased surface temperatures cease is after launch table aspiration when a large portion of the plume is sucked back into the flame trench. Based on the results of the previous sections, it can be seen that the case providing the best hydrogen plume results is Case 4 (base air injection, air curtain and venturi systems). For Case 4, the hydrogen plume produced, and thus the area of elevated surface temperatures, was reduced in size on the launch table opening side of the launch vehicle (see Figure 23 and Figure 24) but the area of increased temperature is larger on the opposite side of the launch vehicle (see Figure 25). It is worth mentioning the base air injection and venturi case, Case 3. The hydrogen plume generated by Case 3 was largely absent from affecting the far side of the launch vehicle (see Figure 22). However, increased surface temperatures and a significant flame were present on the opposite side of the launch vehicle (see Figure 20 and Figure 21).

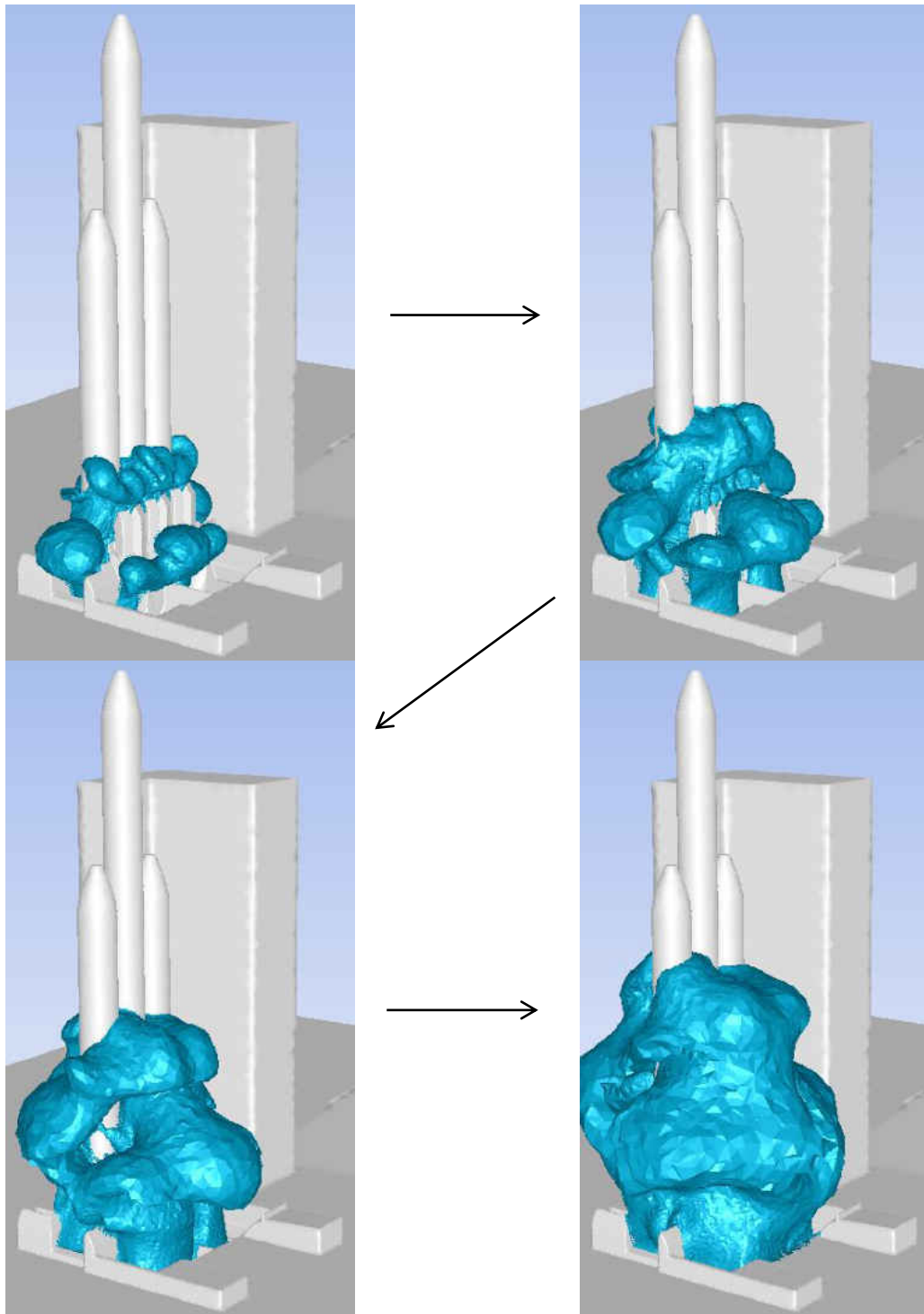


Figure 26: Hydrogen plume rise for the no injection case.

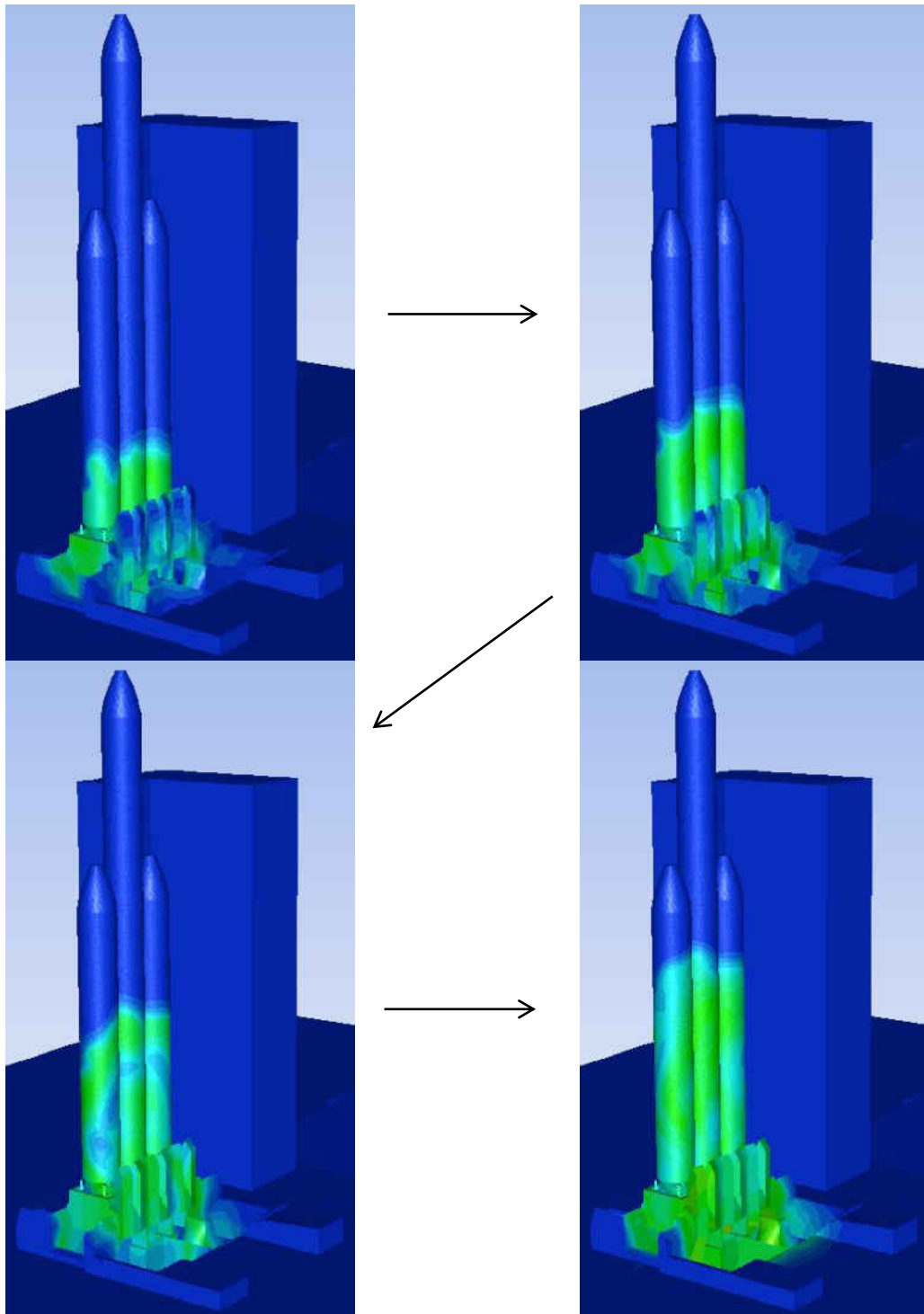


Figure 27: Surface temperature contour plots for the no injection case.

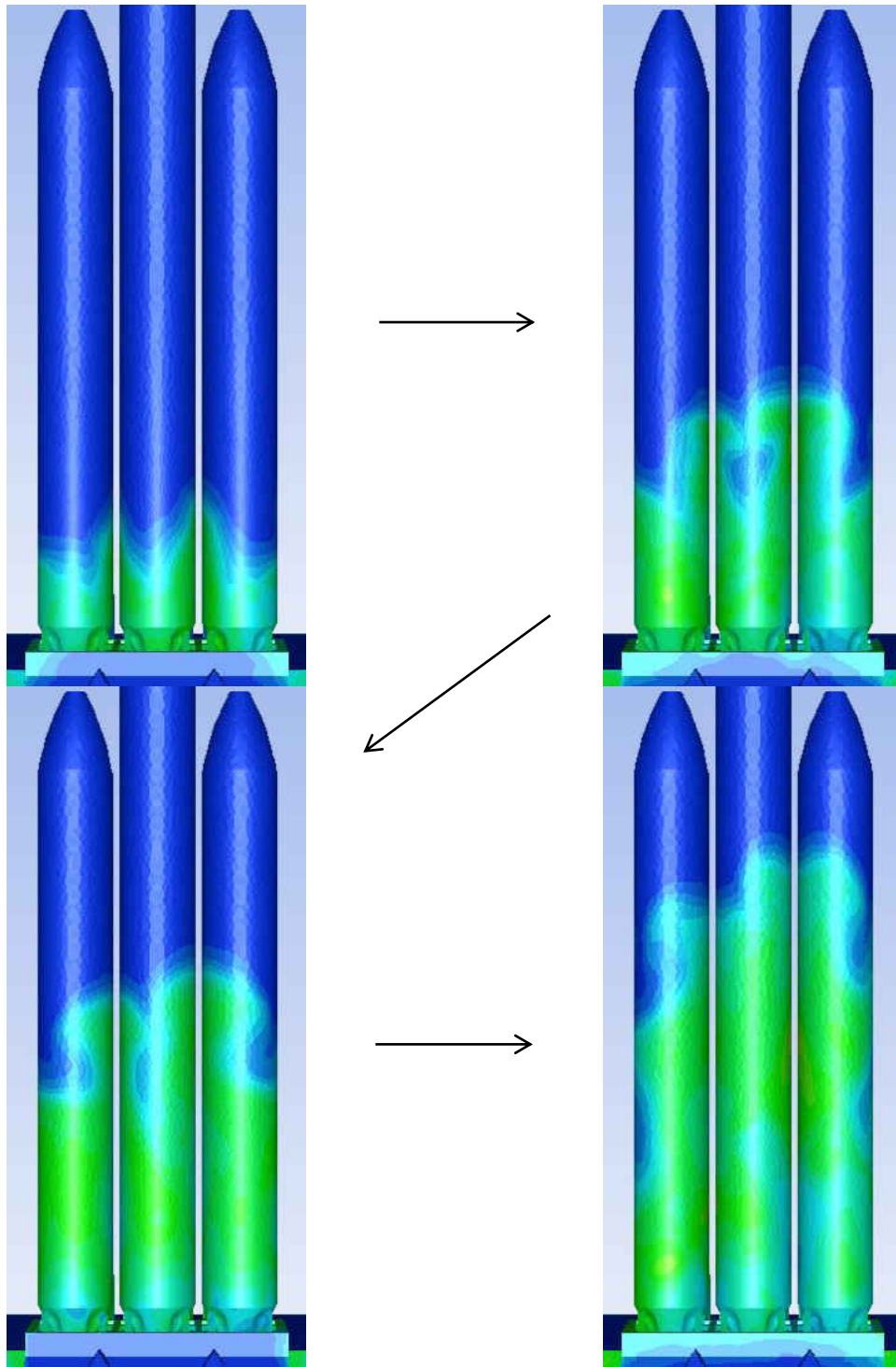


Figure 28: Additional surface temperature contour plots for the no injection case.

Figures comparing Case 3 (base air injection and venturi systems) and Case 4 (base air injection, air curtain and venturi systems) to the no injection case (Case 5) are provided in Figure 29 and Figure 30. Note that each of the snapshots provided in these figures are the final frames taken from each case's respective discussion (Figure 21 and Figure 22, Figure 24 and Figure 25) and that each of the frames occur at the same point in time during the engine start sequence. The impact of the plume mitigation strategies is apparent from the figures; elevated temperatures are seen to be restricted to a lower portion of the launch vehicle for the plume mitigation cases when compared to the case with no mitigation present. Essentially the hydrogen plume rise is delayed but not eliminated with the current plume mitigation air flow rates and configurations.

In the base air injection and venturi case however, one side of the launch vehicle is left nearly untouched by the rising plume (Figure 29, bottom). The other side of the launch vehicle is subject to elevated temperatures but to a much lesser degree when compared to the no injection case. At the time pictured in the upper half of Figure 29, the flame affected area is reduced by approximately 50%. In the base air injection, air curtain and venturi case, the affected area on the same side of the launch vehicle (see upper half of Figure 30) is reduced even further. Unfortunately, the opposite side of the launch vehicle does not fare as well and the plume affected area is only reduced by approximately 30% (see lower half of Figure 30). In addition to the temperature contour plots, a plume size comparison is provided in Figure 31. Based on the temperature contour plots, the injection/venturi case may seem like an improvement over the injection/curtain/venturi case, the plume size in the latter case is more preferable.

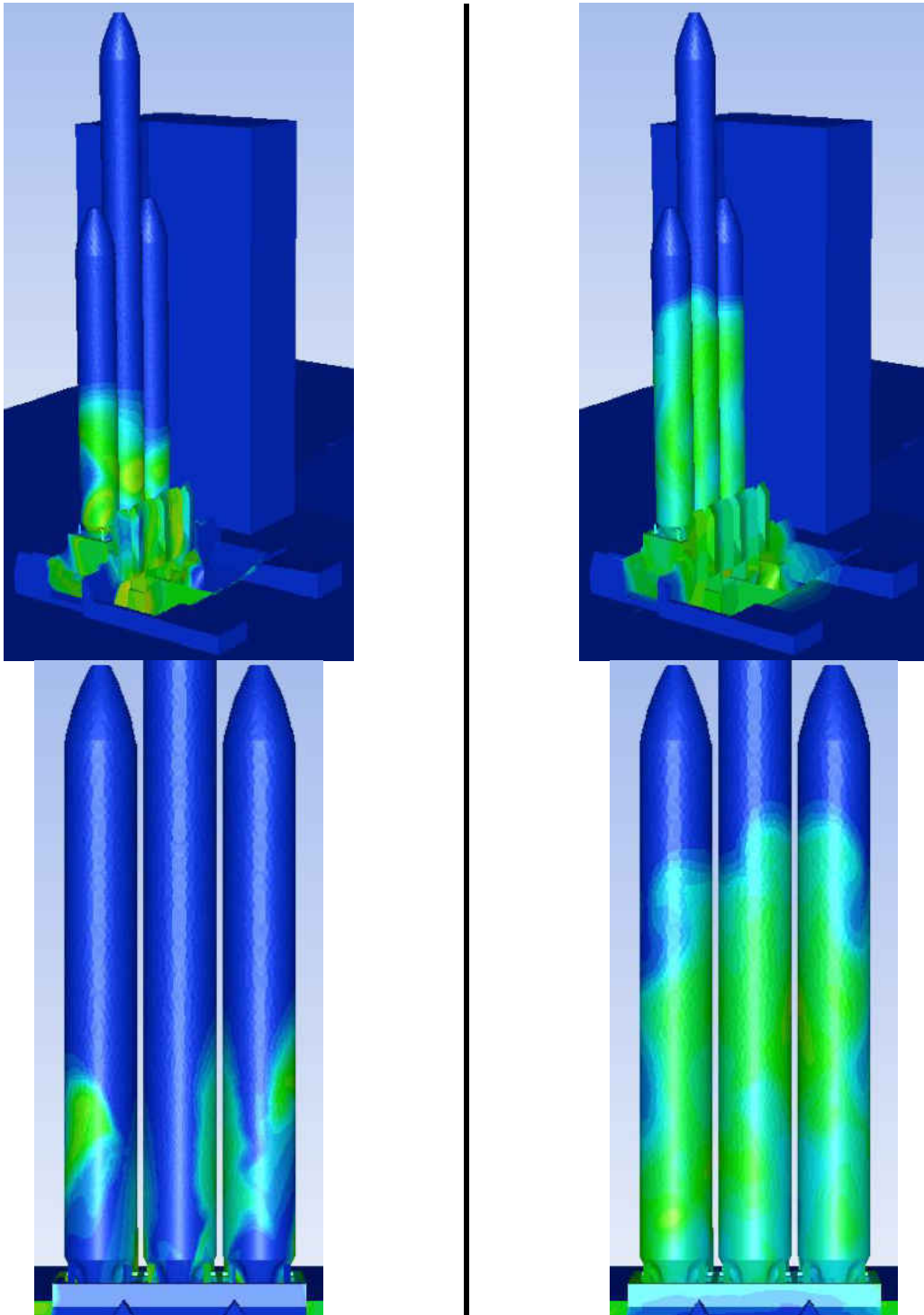


Figure 29: Surface temperature contour plot comparison for the base air injection and venturi case (left column) and the no injection case (right column).

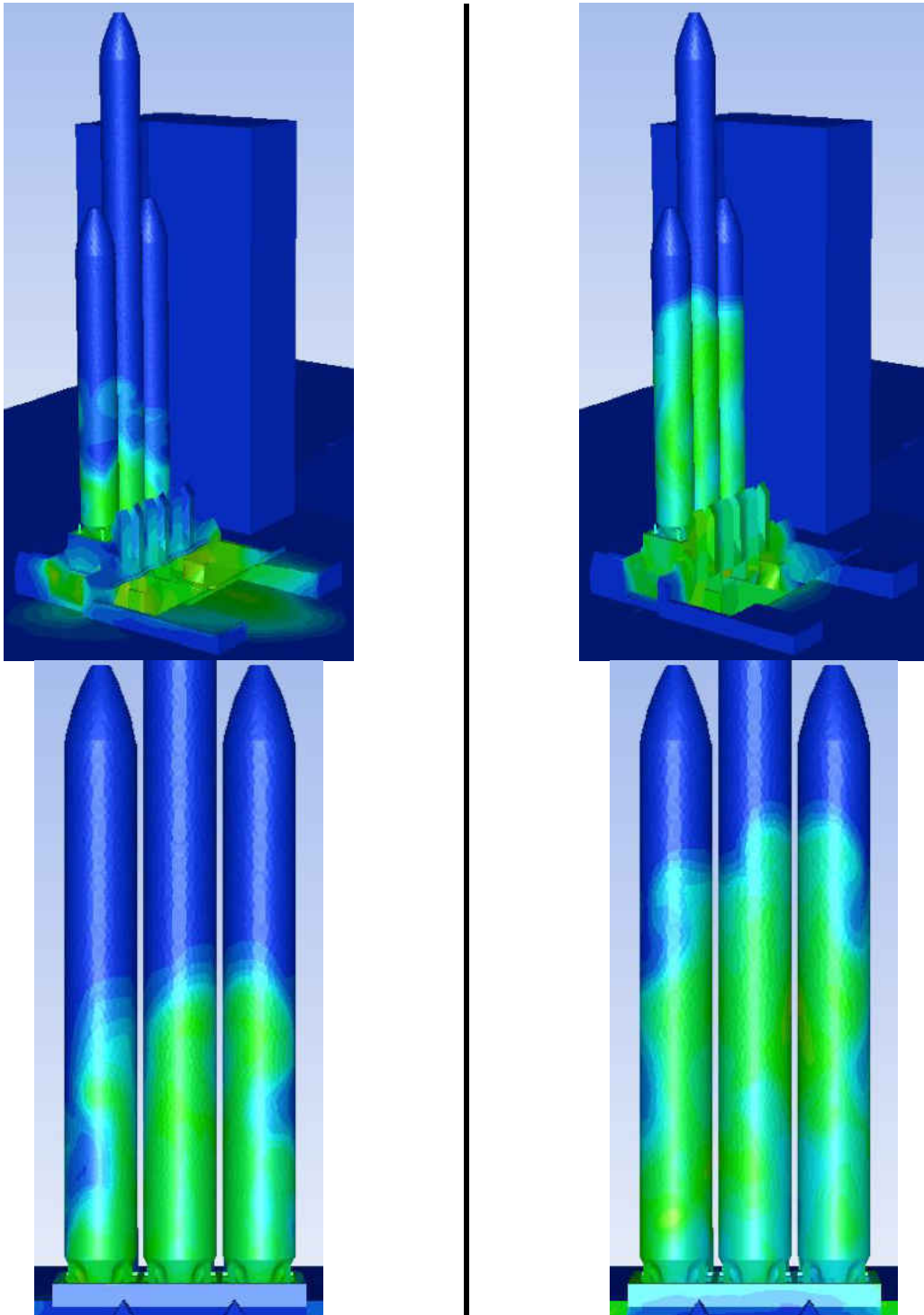


Figure 30: Surface temperature contour plot comparison between the base air injection, air curtain and venturi case (left column) and the no injection case (right column).

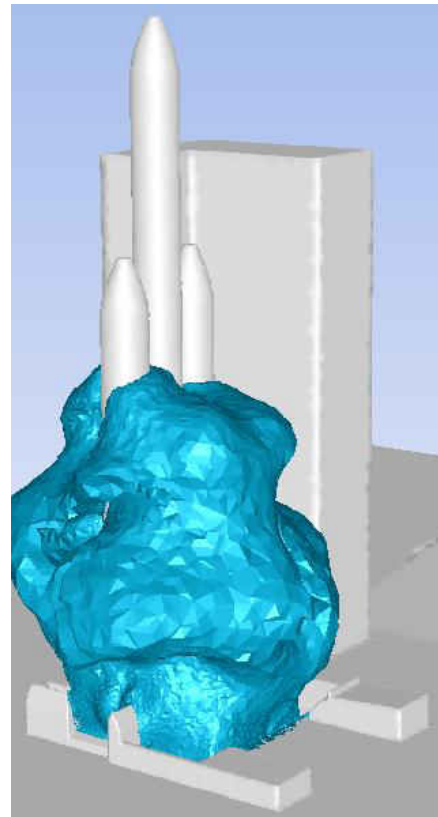
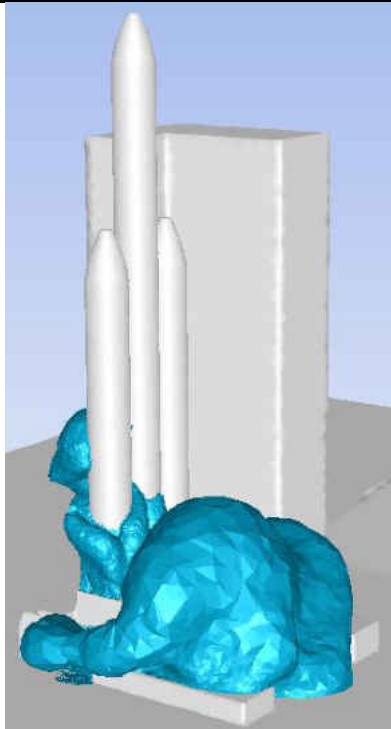
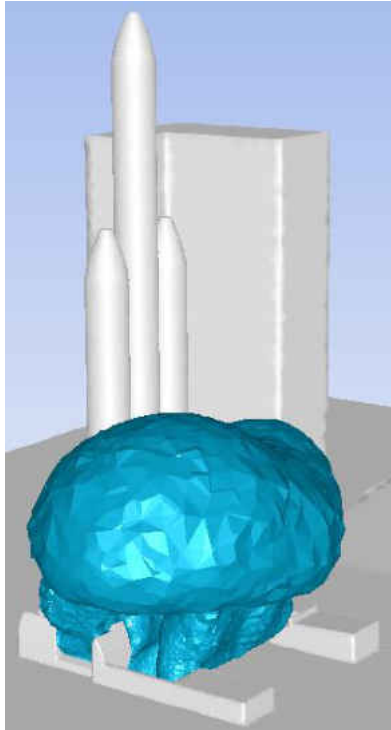


Figure 31: Hydrogen plume rise comparison for the base air injection and venturi case (top left), base air injection, air curtain and venturi case (bottom left) and the no injection case (right).

CHAPTER 4: DISCUSSION AND CONCLUSIONS

During the launch of the United Launch Alliance Delta IV Heavy launch vehicle, a significant flame is produced as a result of excess hydrogen reacting with atmospheric air. In order to address this problem, several mitigation structures were proposed to be added to the existing launch table. These structures were first implemented on a much smaller, reduced model that only included one of the launch vehicle boosters intended to try out various scenarios quickly. The results from the reduced model simulations were then applied to the much more time consuming full scale simulations which included all three of the Delta IV Heavy liquid hydrogen/liquid oxygen powered boosters.

Reduced Model Results

The reduced model proved useful in evaluating the hydrogen plume behavior and a total of 8 separate cases were run, summarized in Table 1, page 21. It was first determined that the inclination angle of the air injection system had a noticeable effect on the amount of flame exiting from the engine section just around the launch vehicle. Of the two injection angles studied (base injection angle and 2.5x base injection angle) it was found that the base injection angle, or the smaller angle with respect to the vertical, resulted in the more favorable plume behavior (see Figure 9, page 22). The base angle was then used for the remaining air injection models.

The next characteristic to be determined was the extent to which the air injection flow rate affected the hydrogen plume behavior. What is the minimum flow rate required to suppress the rising flame? A base flow rate and half of that base flow rate were chosen and applied to the

air injection model. It was shown that the base flow rate outperformed the 0.5x base flow rate air injection case (Figure 10, page 25). It is interesting to note that the approximate equation developed to determine the minimum air injection speed gives an air velocity similar to the air velocity achieved with the 0.5x base air injection flow rate. Consulting Figure 10 shows that the 0.5x base air flow rate is not completely overpowered by the rising plume so the air velocity achieved in that case is near the speed described by the approximate relation.

The final scenario studied on the reduced model was intended to determine the effect several different air curtain flow rates had on the hydrogen plume. One glaring problem evident in the air injection cases was the large flame that rises out of the launch table opening. The air curtain system was used to try and remedy that problem. As expected, a high velocity volume of air resulted in a more favorable hydrogen plume size, shown in Figure 11 on page 27. What was not expected was the air curtain's influence on the plume exiting the launch table around the launch vehicle. The increased air flow into the launch table from the air curtain caused the pressure inside the engine section of the launch table to increase. This increased pressure allowed the flame to more easily escape out of the top of the launch table against the air injection's influence; see the last frames of Figure 11. When the air curtain was scaled up to the full 3 engine model, it was determined that the 1.6x base flow rate air curtain would be difficult to supply realistically. The base air curtain was then chosen to be applied to the full scale VAFB model.

Full Scale Model Results

The full scale VAFB mesh was naturally much larger than the reduced mesh and thus took significantly longer to run. This resulted in a lower number of more focused cases (see Table 2, page 32) that implemented the findings gathered from the reduced model cases. All of the full scale models included a base air injection angle. Additionally, only one air curtain flow rate was brought over from the reduced model cases. The venturi system was not implemented into the reduced model but several steady state simulations were run to assess the effect that the venturi introduction angle had on air flow speed at the launch table. A shallow venturi angle, in line with the flame trench direction, was chosen along with a single flow rate to be applied to the full scale model.

Two cases were worthy of a closer look: Case 3 (base air injection and venturi systems) and Case 4 (base air injection, air curtain and venturi systems) from Table 2. The hydrogen plume and surface temperature behavior of Case 3 at a certain point during the launch timeline is provided below in Figure 32. Case 3 lacks an air curtain system and the resulting plume reflects this fact. Figure 32 (left) shows that a large plume escapes from the launch table opening and is allowed to rise upward. Increased surface temperatures are observed on that side of the launch vehicle (Figure 32, center). Due to the lack of an air curtain system, the air injection system is more effective at suppressing the flame rise through the center section of the launch table and a minimal amount of the launch vehicle's surface is affected by increased temperatures (Figure 32, right).

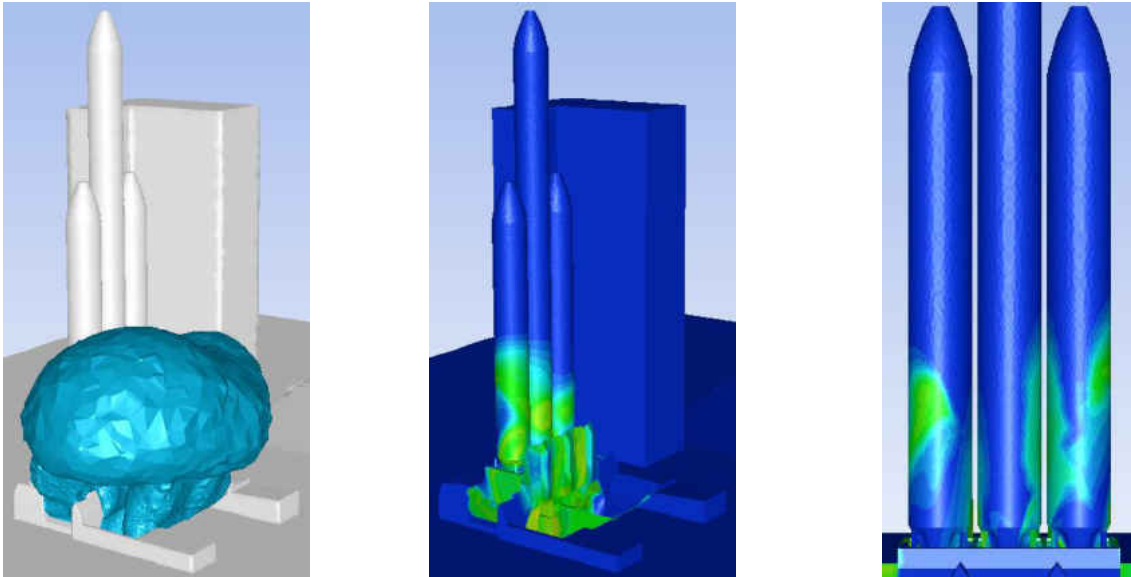


Figure 32: The hydrogen plume (left) and launch vehicle surface temperatures (center, right) for Case 3 in Table 2.

The case that performed the best out of the cases studied was Case 4 from Table 2. This model included each type of plume mitigation strategy proposed: a base flow rate air injection system, an air curtain system, and a venturi system. A summary of the results for hydrogen plume size and surface temperatures are provided in Figure 33. When compared with the no injection case (Figure 26) this case was successful at significantly reducing the hydrogen plume size. While a hydrogen plume is still present, it is far from the size observed when no plume mitigation is present. The plume size reduction yields improved launch vehicle surface temperatures for the side of the launch vehicle pictured in Figure 33 (center). The increased pressure inside of the launch structure from the air curtain system caused the air injection system to lose effectiveness and allows flame to escape the launch table. The impact is shown in Figure 33 (right); elevated temperatures are seen at a higher point on the launch vehicle than the opposite side.

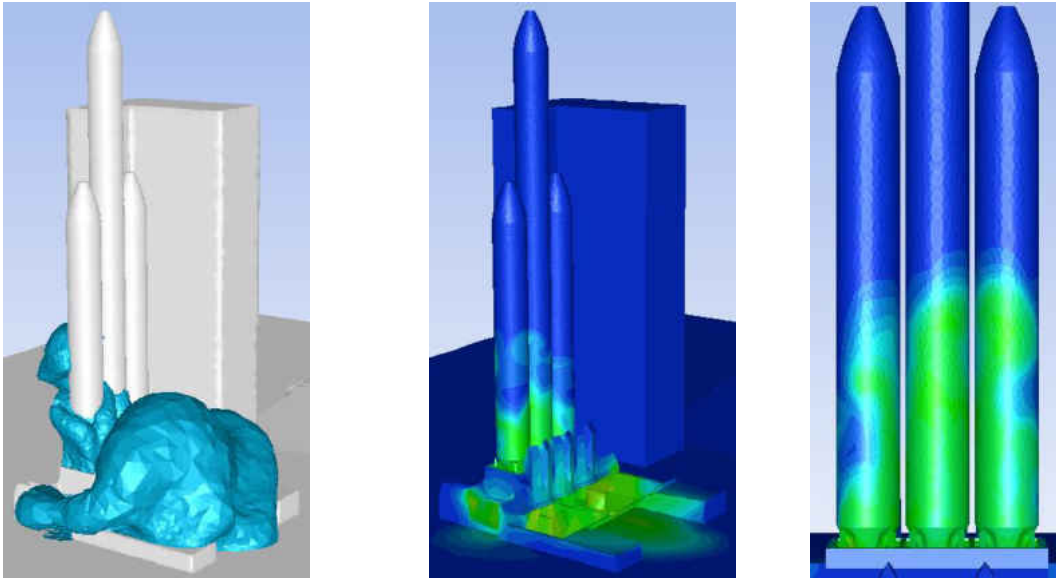


Figure 33: The hydrogen plume (left) and launch vehicle surface temperatures (center, right) for Case 4 in Table 2.

Based on the results summarized here, it is clear that the size of the hydrogen plume generated by the United Launch Alliance Delta IV Heavy launch sequence is reduced when the proposed plume mitigation strategies are employed. Air injection alone can be seen to diminish the size of the hydrogen plume in the vicinity of the launch vehicle but a large flame still exits the large launch table opening. The 1.6x base flow rate air injection case excels at suppressing flame from rising through the launch table near the launch vehicle as shown from the surface temperature plot Figure 16 on page 36. However, the 1.6x base flow rate case suffers from a lack of an air curtain system and increased surface temperatures are present on one side of the launch vehicle. The best plume mitigation results were achieved when an air injection system was used in conjunction with the air curtain and venturi systems. The presence of the air curtain system produced an undesirable increase in the pressure inside of the launch table. This increase in pressure acted against the air injection system and ultimately forced the high temperature water vapor upwards out of the launch table. The air injection system in the air curtain simulations

were seen to perform worse than their equivalent simulations lacking an air curtain. In its current implementation, the air curtain geometry points downward at an angle such that air flow is allowed to enter the open flame trench. One possible solution to this increased pressure problem could be to point the air curtain systems so they create a horizontal barrier rather than inject into the flame trench.

Unfortunately, none of the proposed strategies completely eliminated the plume. Even the air injection, air curtain and venturi system combination is eventually overpowered and flame is allowed to rise out of the launch table. However, the plume that rises is much smaller in size and also has a smaller residence time near the launch vehicle until it is pulled into the launch table due to aspiration from the vehicle engine bulk flow. Overall, the plume mitigation strategies applied resulted in a significant improvement over the case where no mitigation was applied. Possible future work could include larger ranges of air flow rates and mitigation combinations as well as the inclusion of other mitigation strategies currently being developed.

REFERENCES

- [1] B. F. Magnussen and B. H. Hjertager. On mathematical models of turbulent combustion with special emphasis on soot formation and combustion. In *16th Symp. (Int'l.) on Combustion*. The Combustion Institute, 1976.
- [2] Barlow, R.S., A.N. Karpetis, J.H. Frank, and J.-Y. Chen. "Scalar Profiles and NO Formation in Laminar Opposed-flow Partially Premixed Methane/air Flames." *Combustion and Flame* 127.3 (2001): 2102-118. Web.
- [3] "FLUENT 6.3 Documentation." *FLUENT 6.3 Documentation*. N.p., n.d. Web.
<<http://aerojet.engr.ucdavis.edu/fluenthelp/index.htm>>.
- [4] Rose, J. W., Henry Michael Spiers, and J. R. Cooper, eds. "Technical data on fuel." British National Committee, World Energy Conference, 1977.
- [5] McBride, Bonnie J., Sanford Gordon, and Martin A. Reno. "Coefficients for Calculating Thermodynamic and Transport Properties of Individual Species." *Unknown* (1993): n. pag. Print.
- [6] Faghri, Amir, Yuwen Zhang, and John R. Howell. *Advanced Heat and Mass Transfer*. Columbia, MO: Global Digital, 2010. Print.
- [7] Turns, Stephen R. *An Introduction to Combustion: Concepts and Applications*. New York: McGraw-Hill, 2012. Print.
- [8] Sutton, George Paul., and Oscar Biblarz. *Rocket Propulsion Elements*. New York: John Wiley & Sons, 2001. Print.

- [9] Klein, H.H, P.C. Chan, and R.K.-C Chan. "JAYCOR CFD Analysis of the Hydrogen Disposal System at the Vandenberg Space Shuttle Launch Site." *American Institute of Aeronautics and Astronautics* (1989): n. pag. Web.
- [10] Schmitt, D.A., and Gordon Sholes. "Large Scale Tests of a Steam Inerting System for Unburned Hydrogen in a Closed Exhaust Duct." *American Institute of Aeronautics and Astronautics* (1988): n. pag. Web.
- [11] Canabal, Francisco, and Abdelkader Frendi. "Study of the Ignition Overpressure Suppression Technique by Water Addition." *Journal of Spacecraft and Rockets* 43.4 (2006): 853-65. Web.
- [12] Ikawa, Hideo, and Fred S. Laspesa. "Ignition/Duct Overpressure Induced by Space Shuttle Solid Rocket Motor Ignition." *American Institute of Aeronautics and Astronautics* (1985): n. pag. Web.
- [13] Saito, Takao, Tetsuya Nakamura, Munetsugu Kaneko, Igor Men'shov, and Yoshiaki Nakamura. "Numerical Investigation of SRB Ignition Overpressure." *American Institute of Aeronautics and Astronautics* (2004): n. pag. Web.
- [14] Magnussen, Bjorn F. *On the Structure of Turbulence and a Generalized Eddy Dissipation Concept for Chemical Reaction in Turbulent Flow*. Proc. of 19th American Institute of Aeronautics and Astronautics Aerospace Science Meeting, Missouri, St. Louis. N.p.: n.p., n.d. Print.